CHALMERS
UNIVERSITY OF TECHNOLOGY

CFD modeling of the Neutral Atmospheric Boundary Layer above Inhomogeneous forest

Master's thesis in Applied Mechanics

ALFRED ANDREW KLERUU

Department of Mechanics and Maritime Sciences
CHALMERS UNIVERSITY OF TECHNOLOGY
Gothenburg, Sweden 2020

Master's thesis 2020:06

CFD modeling of the Neutral Atmospheric Boundary Layer above Inhomogeneous forest

ALFRED ANDREW KLERUU

CHALMERS
UNIVERSITY OF TECHNOLOGY

Department of Mechanics and Maritime Sciences
Division of Fluid Dynamics
Chalmers University of Technology
Gothenburg, Sweden 2020

CFD modeling of the Neutral Atmospheric Boundary Layer above Inhomogeneous forest
Alfred Andrew Kleruu

Supervisor: Hamidreza Abedi, Division of Fluid Dynamics
Examiner: Lars Davidson, Division of Fluid Dynamics

Master's Thesis 2020:06
Department of Mechanics and Maritime Sciences
Division of Fluid Dynamics
Chalmers University of Technology
SE-412 96 Gothenburg
Telephone +46 31 772 1000

Typeset in LaTeX
Gothenburg, Sweden 2020

CFD modeling of the Neutral Atmospheric Boundary Layer above Inhomogeneous forest

ALFRED ANDREW KLERUU
Department of Mechanics and Maritime Sciences
Chalmers University of Technology

Abstract

Homogeneous assumption of distribution of forest canopy has been a keen study in several works in assessing the effect of forest canopy on the mean velocity profile and turbulence within a wind farm. While this assumption plays a vital role in wind energy assessment, it doesn't represent the realistic approach given by the inhomogeneous (heterogeneous) assumption. In this study the Large-Eddy Simulation (LES) is used to model the neutral Atmospheric Boundary Layer (ABL) over a heterogeneous forest wind farm. This is done by utilizing the power of the Computational Fluid Dynamics (CFD) tool, *STAR-CCM+* software. Thereafter the structural dynamic response of the wind turbines are assessed using the aero-elastic solver *FAST*. Comparisons are made between two simulation cases (heterogeneous versus homogeneous forest canopy distribution) and it is seen that the homogeneous forest assumption over-predicts turbulent kinetic energy levels the wind turbines are subjected to compared to the heterogeneous forest assumption.

Keywords: Wind turbine, Atmospheric boundary layer, Large-Eddy Simulation, Homogeneous forest, Inhomogeneous forest, *STAR-CCM+*, *FAST*.

Acknowledgements

I would like to extend my deepest gratitude to Hamidreza Abedi for first letting me take part in this project which turned out to be my thesis work and for his support and guidance throughout its course. I am thankful to my examiner Lars Davidson for his support and directives. I met lots of awesome people at the Department of Mechanics and Maritime Sciences who made my time fruitful and memorable, I would like to thank all of them. I would also like to thank Guglielmo Minelli, Asuka Pietroniro, Omar Fares, Johannes Dwalibi and Adam Jareteg who I met at the Division of Fluid Dynamics for the insightful discussions we had and help they extended to me. My gratitude extends to all the people at the division who by one way or another we crossed path and made life at the division fruitful, easier and fun, your support is truly appreciated. Furthermore, I would like to thank my family and friends for their support and for being there for me. Finally special thanks goes to my mother for her continuous unconditional love and support.

Alfred Andrew Kleruu, Gothenburg, April 2020

Contents

Nomenclature **xiv**

List of Figures **xv**

List of Tables **xvii**

1 Introduction **1**
1.1 Objectives . . . 1
1.2 Literature Review . . . 2
1.3 Röbergskullen Wind Farm . . . 2

2 Theory **3**
2.1 Atmospheric Boundary Layer (ABL) . . . 3
2.2 Physics and Governing Equations . . . 4
2.2.1 The Coriolis force . . . 5
2.3 Computational Fluid Dynamics (CFD) . . . 5
2.3.1 Turbulence Modeling . . . 6
2.3.1.1 Reynolds Averaged Navier-Stokes Equations (RANS) model . . . 6
2.3.1.2 Eddy Viscosity Models (EVM) . . . 7
2.3.1.3 Reynolds Stress Transport Models (RSM) . . . 8
2.3.1.4 Large-Eddy Simulation(LES) . . . 9
2.3.1.5 Initialization and Inflow for LES . . . 11
2.3.2 Wall Treatment . . . 11
2.4 Modeling the Atmospheric Boundary Layer (ABL) . . . 12
2.5 Forest Modeling . . . 14
2.6 Numerical Methods . . . 14
2.6.1 Properties of Numerical Solution Methods . . . 14
2.6.1.1 Consistency . . . 14
2.6.1.2 Stability . . . 15
2.6.1.3 Convergence . . . 15
2.6.1.4 Conservation . . . 15
2.6.1.5 Boundedness . . . 15
2.6.1.6 Realizability . . . 16
2.6.1.7 Accuracy . . . 16
2.6.2 Discretization Schemes . . . 16
2.6.2.1 Finite Difference (FD) . . . 16

2.6.2.2 Finite Volume (FV) . . . 17
2.6.2.3 Finite Element (FE) . . . 17
2.7 Wind Energy . . . 17
2.7.1 Wind Turbine Structure . . . 17
2.7.2 Wind Turbine Aerodynamics . . . 19
2.7.2.1 Blade Element Momentum Theory (BEMT) . . . 20
2.7.3 Blade Pitch Control . . . 21
2.7.4 5-MW Reference Wind Turbine . . . 22

3 Methodology **25**
3.1 Computational Domain . . . 25
3.2 Topography and Plant Area Density (PAD) . . . 27
3.3 Mesh . . . 28
3.4 LES Simulation Setup . . . 28
3.5 Aero-elastic Simulation Setup . . . 29

4 Results **31**
4.1 LES Simulation . . . 31
4.2 Wind Turbine Structural Dynamic Response . . . 36

5 Conclusion **45**

Bibliography **47**

A Appendix 1 **I**
A.1 Wind Measurements over Rödbergskullen Wind Farm . . . I

Nomenclature

Abbreviations

ABL Atmospheric Boundary Layer

a.g.l above ground level

BEMT Blade Element Momentum Theory

CAE Computer Aided Engineering

CFD Computational Fluid Dynamics

DNS Direct Numerical Simulation

FAST Fatigue, Aerodynamics, Structures and Turbulence

LAD Leaf Area Density

LES Large Eddy Simulation

NREL National Renewable Energy Laboratory

PAD Plant Area Density

RANS Reynolds Averaged Navier-Stokes

SGS Subgrid Scale

WALE Wall-Adopting Local Eddy

Greek Letters

Δ Filter width

ν Kinematic viscosity

ν_{SGS} Subgrid scale viscosity

ν_T Turbulent eddy viscosity

μ Dynamic viscosity

ρ Density

κ von Karman constant

δ_{ij} Dirac delta operator

ϵ Turbulent dissipation

τ_{ij} Subgrid Scale stresses

σ' Local solidity

Ω_j Angular velocity vector of the Earth's rotation

ω Angular velocity of the Earth

ϕ Latitude

ϵ_{ijk} Permutation tensor

σ_ϵ $k-\epsilon$ model constant

σ_k $k-\epsilon$ model constant

π Pi

κ_C Cut-off wavenumber

τ_w Wall shear stress

Roman Letters

C_D Drag coefficient

C_L Lift coefficient

C_s Smagorinsky constant

C_μ $k-\epsilon$ model constant

$C_{\epsilon 1}$ $k-\epsilon$ model constant

$C_\epsilon 2$ $k-\epsilon$ model constant

E Wall function coefficient

F_i Aerodynamic drag

f_C Coriolis parameter

f_S van Driest Damping function

f Roughness function

G Filter function

g Acceleration due to gravity

k Turbulent kinetic energy

l Turbulent length scale

p Pressure

$\overline{p}$ Resolved pressure

y_0 Roughness height

R^+ Roughness parameter

S Strain rate

t Time

u Velocity

$\overline{u}$ Resolved velocity

u_τ Wall friction velocity

u^+ Non-dimensional velocity

x, y, z Cartesian coordinates

y Wall distance, vertical direction

y^+Non-dimensional wall distance

List of Figures

2.1 The Atmospheric Boundary Layer 4
2.2 Energy Spectrum 9
2.3 The Wall Region 12
2.4 Horizontal Axis Wind Turbine 19
2.5 Wind Turbine Rotor with incoming flow 20
2.6 Schematic of Blade Element Theory of an airfoil subjected to aerodynamic forces 20
2.7 Steady-state operating condition responses for the NREL offshore 5-MW Baseline Wind Turbine 23

3.1 The Computational Domain 26
3.2 Homogeneous forest LAD profile 27

4.1 Streamwise mean velocity profile of Homogeneous (left) and Heterogeneous (right) forest. 31
4.2 Forest Height map of the heterogeneous forest. 32
4.3 Vertical mean velocity profile of Homogeneous (left) and Heterogeneous (right) forest. 32
4.4 Spanwise mean velocity profile of Homogeneous (left) and Heterogeneous (right) forest. 33
4.5 TKE profile of Homogeneous (left) and Heterogeneous (right) forest. . 33
4.6 Normal Reynolds stresses $< \overline{u}'\overline{u}' >$ in the streamwise direction of Homogeneous (left) and Heterogeneous (right) forest. 34
4.7 Normal Reynolds stresses $< \overline{v}'\overline{v}' >$ in the vertical direction of Homogeneous (left) and Heterogeneous (right) forest 34
4.8 Normal Reynolds stresses $< \overline{w}'\overline{w}' >$ in the spanwise direction of Homogeneous (left) and Heterogeneous (right) forest 34
4.9 Shear Reynolds stresses $< \overline{u}'\overline{v}' >$ of Homogeneous (left) and Heterogeneous (right) forest 35
4.10 Shear Reynolds stresses $< \overline{u}'\overline{w}' >$ of Homogeneous (left) and Heterogeneous (right) forest 35
4.11 Shear Reynolds stresses $< \overline{v}'\overline{w}' >$ of Homogeneous (left) and Heterogeneous (right) forest 36
4.12 Mean and Standard deviation of streamwise velocity $\overline{u}$ at the hub height of Homogeneous (top) and Heterogeneous (bottom) forest. . . 37
4.13 Mean and Standard deviation of vertical velocity $\overline{v}$ at the hub height of Homogeneous (top) and Heterogeneous (bottom) forest. 38

4.14 Mean and Standard deviation of spanwise velocity $\overline{w}$ at the hub height of Homogeneous (top) and Heterogeneous (bottom) forest. 39
4.15 Mean and Standard deviation of blade pitch angles of Homogeneous (top) and Heterogeneous (bottom) forest. 40
4.16 Mean and Standard deviation of generated rotor torque of Homogeneous (top) and Heterogeneous (bottom) forest. 41
4.17 Mean and Standard deviation of rolling moment (Mx) for Homogeneous (top) and Heterogeneous (bottom) forest. 42
4.18 Mean and Standard deviation of pitching moment (My) for Homogeneous (top) and Heterogeneous (bottom) forest. 43
4.19 Mean and Standard deviation of yawing moment (Mz) for Homogeneous (top) and Heterogeneous (bottom) forest. 44

A.1 Wind speed average measurements over Rödbergskullen. The figure shows overall recorded values and compares them to the values recorded only during the day and during the night. The blue lines indicate measured values while the red lines indicate 72 hour average. I
A.2 Histogram of recorded wind speed averages II
A.3 Wind Direction II
A.4 Turbulent Intensity III
A.5 Topography of the area III

List of Tables

2.1 Properties of the 5-MW NREL Reference Wind Turbine Model 22

3.1 Locations of Met mast and wind turbines in the domain 26
3.2 Elevations from the ground of each individual wind turbine 27
3.3 Initial conditions and fluid properties 28
3.4 Coefficients 28
3.5 Boundary conditions 29

1
Introduction

With the ongoing changes in the climate, further developments of the renewable energy sources are inevitable . Wind energy is among these sources. Wind turbines operate within the Atmospheric Boundary Layer (ABL) and they are always subjected to atmospheric turbulence. Accurate predictions of the wind flow patterns is crucial for design purposes which in turn the fatigue life of a turbine can be assessed. The fatigue analysis leads to optimizing the design and operation of a wind turbine which accordingly increases the operating life of a wind turbine.

On-site measurements are usually preferred but they come in short as they are sparse. On top of that on-site measurements include many atmospheric factors taking place at the same time and it can be difficult to isolate them and focus on a specific factor. This is where the capability of simulation tools such as Computational Fluid Dynamics (CFD) comes in. However how well these tools give out correct prediction depend on many numerical and modeling assumptions [3]. Furthermore depending on where a wind turbine is located whether on flat or on complex terrain, dense or less dense forest areas, the simulations will yield different results.

In Sweden, wind farms are located mostly in forest areas [19]. The forest distribution has an effect on the flow field of the wind patterns blowing to the wind farm. Several studies have modeled forest with the homogeneous assumption.

This study will focus on the impact of the inhomogeneous (heterogeneous) forest canopy on the mean velocity profile and turbulence on a wind farm. Thereafter it will be compared to the homogeneous forest assumption.

1.1 Objectives

The aim of this study is to assess the effect of the heterogeneous forest on the mean velocity profile and turbulent kinetic energy of wind flow field on a wind farm and study the structural dynamic response of wind turbines.

This study uses the CFD tool *STAR-CCM+* for the flow simulation and uses the aero-elastic solver *FAST* to study the structural dynamic response of the wind turbine. *FAST* is *NREL's* primary Computer Aided Engineering (CAE) tool for the coupled dynamic response of wind turbines. It consists of aerodynamic, hydrody-

namic models, control and electrical dynamic models and structural (elastic) models for aero-hydro-servo-elastic simulation in the time domain [17].

1.2 Literature Review

Modeling flow within the ABL and assessing the effect of local topography on the mean velocity field and turbulence has been the subject of several studies. Perhaps one of the most widely used test case is that of the Askervein hill located at the Hebrides where intensive field measurements have been done. The measurements have helped in making comparisons with simulations as well as validating turbulence models to be used in modeling flow over complex terrains [20] [21].

On the subject of validating atmospheric boundary layer flows, a study by Bechmann [3] focused on validating and developing a turbulence model for such flows using Large-Eddy Simulation (LES). Since LES can not handle the rough surface of the earth well, with reasonable computational expense it was coupled with RANS to form a hybrid model where the former would handle the outer flow while the latter would handle the near ground region. Similar to this study, a study by Kandt [14] focused on modeling the the ABL for an offshore environment using LES and comparing the results with results from spectral flow field.

Brekason [4] generated a transient CFD model of the ABL to study the effects of the complex terrain on the mean flow field and the dynamic response of a wind turbine. He concluded that placing a wind turbine in a complex terrain topography results into higher fatigue levels on a wind turbine compared to placing it on a flat terrain.

Nebenführ and Davidson [18] modeled the neutral atmospheric boundary layer over a sparse and dense forest as well as over grass covered flat terrain and studied the dynamic structural response of a generic wind turbine. Indeed they observed increased fatigue levels over the two forest.

1.3 Röbergskullen Wind Farm

The Rödbergskullen wind farm is used in this study. It is considered as a complex terrain covered by a forest with a heterogeneous distribution. The heterogeneous distribution of the forest over the wind farm makes it an ideal location to conduct this study. The wind farm is located 100km north of Karlstad, Sweden 540m above sea level. It is comprised of eight Vestas V90 horizontal axis wind turbines, each with a capacity of 2MW. The hub height is 80m and the rotor diameter is 90m giving a total height of 125m. Field measurements from this wind farm were also taken prior to this study for comparison purposes [4].

2

Theory

2.1 Atmospheric Boundary Layer (ABL)

This is the lowest part of the atmosphere which is in contact with the Earth's surface. The flow field in this layer of the atmosphere is affected by the Earth's surface. In this layer friction and temperature effects dominate the flow and create atmospheric turbulence . Beyond this layer rotational effects are observed and dominate the flow rather than turbulence. It is why that at the very top of this layer the wind speed equals to that of the geostrophic wind and at the ground levels where turbulence is more observed wind speed goes to zero with a logarithmic profile [3].

The height of the ABL and the size of the turbulent scales greatly depends on the thermal stratification which depends on the part of the day. During the day surface heating causes large thermal motions which increase the height of the ABL up to heights of 3000m. This is the unstable stratification and turbulence is amplified with altitude. During the night the situation is reversed and cooling of the surface occurs which results in decrease of size of the turbulent scales and consequently the height of the ABL can decrease to heights of 100m. This is the stable stratification. Another situation occurs during the late afternoon when there strong winds, in this case turbulence is generated through wind gradients rather than due to surface heating and this is the neutral Stratification. In this study the modeling is limited to the neutral atmospheric boundary layer [3].

Due to balance of pressure, friction and Coriolis forces the wind speed and direction vary throughout the ABL. The ABL can be decomposed into two sublayers; the surface layer (SL) and the outer layer. The surface layer is the lowest and inner part of the ABL where the turbulent fluxes can be considered constant and Coriolis force is negligible. In the surface layer, the surface effects like friction and heating dominate and it has roughness elements like trees. It is within this sublayer where different engineering structures are located such as buildings [3]. A picture depicting the ABL is shown below in Fig. 2.1.

The pressure decreases within the ABL according to the following formulation.

$$\frac{\partial p}{\partial z} = -\rho g \tag{2.1}$$

where g, ρ and z are the acceleration due to gravity, the fluid density and altitude respectively. If an air element is lifted up in the atmosphere, its pressure will decrease

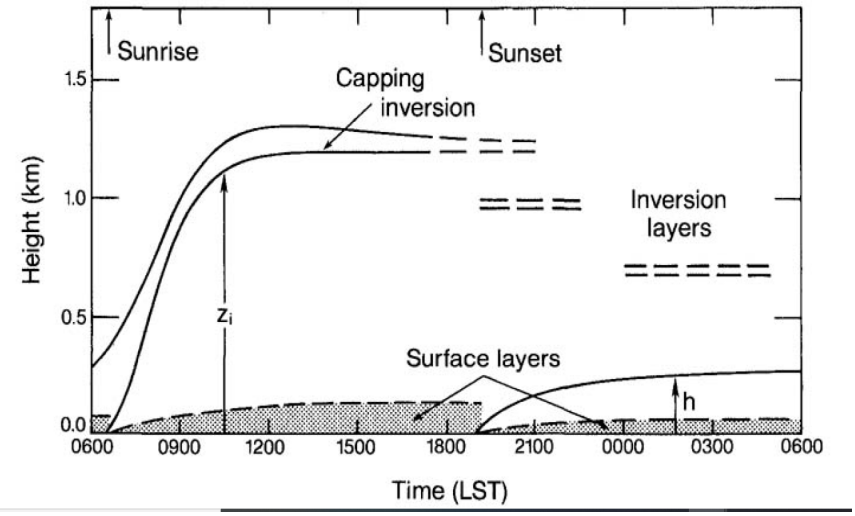

Figure 2.1: The Atmospheric Boundary Layer [13].

following Eq. 2.1 and its temperature will decrease too.

2.2 Physics and Governing Equations

The mathematical description and the physics of the flow field come from the three fundamental equations of motion. The continuity equation, the momentum equation (the Navier-Stokes equation) and the energy equation. However the are several assumptions which are taken to account in this study.

- Energy transfer is considered negligible and so the third equation (energy equation) can be omitted.
- The flow is considered incompressible and the fluid (air) is considered Newtonian.
- Viscosity and temperature are considered to be constant.
- The effect of the wake of a wind turbine and its influence on other wind turbines in the wind farm is neglected. (Only the wind flow is simulated).
- The ABL modeling is considered to be that of the neutrally stratified condition.

The original statement of the continuity and Navier-Stokes equations of are described in Eq. 2.2 and Eq. 2.3 while considering the assumptions above;

$$\frac{\partial u_i}{\partial x_i} = 0 \tag{2.2}$$

$$\frac{\partial u_i}{\partial t} + u_j \frac{\partial u_i}{\partial x_j} = -\frac{1}{\rho}\frac{\partial p}{\partial x_i} + \nu \frac{\partial^2 u_i}{\partial x_j \partial x_j} + F_i \tag{2.3}$$

where u_i, p, t, x, F_i, and ν are the velocity, pressure, time, the spatial coordinate, the aerodynamic drag force imposed by the forest and the kinematic viscosity respectively.

2.2.1 The Coriolis force

Effects of the earth's rotation are observed when simulating the ABL and hence the Coriolis force. The Coriolis force appears in the equations of motion only in the non-inertial coordinate system. Motion is considered in a moving reference given by the earth's rotation and hence the Coriolis force is required. The height of the ABL to the point whereby the flow velocity equals to that of geostrophic wind is given by,

$$h = C\left(\frac{u_\tau}{f_C}\right) \tag{2.4}$$

where u_τ is the friction velocity, C is a constant often chosen to be 0.3 and f_C is the Coriolis parameter which accounts for earth's rotation. The Coriolis force per unit mass is given by, $F_{CORIOLIS} = -2\epsilon_{ijk}\Omega_j u_k$ where Ω_j is the angular velocity vector of the earth's rotation, u_k is the velocity in the rotating system and ϵ_{ijk} is the permutation tensor. The components of Ω_j are given by $\Big[0, \omega cos(\phi), \omega sin(\phi)\Big]$ where ϕ is the latitude and ω is the angular velocity of the earth ($7.27 \times 10^{-5} s^{-1}$) respectively. The Coriolis parameter can be defined as $f_C = 2\omega sin(\phi)$. The traditional value of f_C normally used is $10^{-4} s^{-1}$ which corresponds to a latitude of $44°N$ [3] [13].

However for this study the Coriolis effect is neglected due to the use of symmetric boundary conditions in STAR-CCM+. If cyclic conditions are used instead then the Coriolis effect could be implemented.

2.3 Computational Fluid Dynamics (CFD)

A branch of fluid dynamics concerned with analyzing and solving different cases of fluid flow using numerical simulation is known as Computational Fluid Dynamics (CFD). The flow field is described with the mathematical description such as the equations of motion. The flow is generally considered as a continuum. CFD aims to solve the flow field numerically with given equations with appropriate initial and boundary conditions to replicate the actual flow at discrete points. Variables such as pressure, velocity and temperature are tracked over the time to represent the flow physics. CFD however relies on experimental measurements and theoretical solutions for validation.

In general numerical analysis of fluid flows follow the following steps;

1. Decide on the physical phenomena you want to analyze and solve. Make the necessary assumptions to replicate the physics of interest. In this study the Large-Eddy Simulation model (LES) is chosen as an appropriate turbulence

model.

2. Discretize the governing equations with one of the discretization schemes; finite difference, finite volume or finite element method and choose the appropriate spatial and temporal resolution.

3. Post-processing the results. The solutions from CFD simulations can be analyzed with different visualization techniques to understand the flow motion. [6]

2.3.1 Turbulence Modeling

As pointed out earlier the ABL turbulence influences the flow field hence an accurate description of the turbulent flow field is inevitable. Direct Numerical Simulation (DNS) is one of the way that solves turbulent flows numerically solving the Navier-Stokes equations with no turbulence models. It is desired to use DNS but it is computationally too expensive to resolve all the scales of turbulence. Most of the time the large scales of turbulence scales are the ones of more interest. Apart from the LES model there are other turbulence models which will be briefly described in this report too.

2.3.1.1 Reynolds Averaged Navier-Stokes Equations (RANS) model

This approach involves breaking down the instantaneous velocity into the sum of its mean and its fluctuating part.

$$u_i = \overline{u}_i + u_i' = U_i + u_i' \tag{2.5}$$

where U_i is the mean velocity field and u_i' is the fluctuating part. $(\bar{\cdot})$ denotes the time-averaged symbol.

This is what is known as the Reynolds decomposition. Substituting Eq. 2.5 this into the equations of motion and time-averaging give the Reynolds Averaged Navier-Stokes (RANS) equations gives,

$$\frac{\partial U_i}{\partial x_i} = 0 \tag{2.6}$$

$$\frac{\partial U_i}{\partial t} + U_i \frac{\partial U_j}{\partial x_j} = -\frac{1}{\rho}\frac{\partial \overline{p}}{\partial x_i} + \nu \frac{\partial^2 U_i}{\partial x_j \partial x_j} - \frac{\partial}{\partial x_j}\overline{u_i' u_j'} \tag{2.7}$$

Equation 2.7 is similar to the Navier-Stokes Eq. 2.3 except with an additional term $\overline{u_i' u_j'}$ which is known as the Reynolds stress term. Turbulence modeling is all about modeling this term by means of known quantities. The Reynolds stress term is a tensor which has 9 components;

$$\begin{pmatrix} \overline{u'u'} & \overline{u'v'} & \overline{u'w'} \\ \overline{v'u'} & \overline{v'v'} & \overline{v'w'} \\ \overline{w'u'} & \overline{w'v'} & \overline{w'w'} \end{pmatrix}$$

$\overline{u'u'}$, $\overline{v'v'}$ and $\overline{w'w'}$ are the normal Reynolds stresses while $\overline{u'v'}$, $\overline{v'w'}$ and $\overline{u'w'}$ are the shear Reynolds stresses.

The two major approaches in RANS turbulence modeling are; the Eddy viscosity models and the Reynolds stress transport models.

2.3.1.2 Eddy Viscosity Models (EVM)

This model uses the concept of turbulent eddy viscosity ν_T to model the stress tensor as a function of mean flow quantities.

From the Boussineq approximation the Reynolds stresses can be expressed as;

$$\overline{u_i'u_j'} = \frac{1}{3}\delta_{ij}k - 2\nu_T\overline{S}_{ij} \tag{2.8}$$

where ν_T , k, δ_{ij} and $\overline{S}_{ij}$ denote the turbulent eddy viscosity, the turbulent kinetic energy, Kronecker delta and strain rate or deformation tensor, respectively.

$\overline{S}_{ij}$ can be expressed as;

$$\overline{S}_{ij} = \frac{1}{2}(\frac{\partial U_i}{\partial x_j} + \frac{\partial U_j}{\partial x_i}) \tag{2.9}$$

and k can be expressed as;

$$k = \frac{1}{2}\overline{u_i'u_i'} \tag{2.10}$$

Among various eddy viscosity models, here only the k-ϵ model is highlighted.

The k-ϵ model is a two-equation turbulence model that uses turbulent kinetic energy, k and turbulent dissipation rate, ϵ to compute the turbulent eddy viscosity ν_T. Turbulent kinetic energy per unit mass can be expressed as the half the sum of the squares of the normal Reynolds stresses.

$$k = \frac{1}{2}(\overline{u_1'}^2 + \overline{u_2'}^2 + \overline{u_3'}^2) \tag{2.11}$$

The idea is to use two global variables that represent turbulence structure of the flow to model. The two global variables are length scale l and and time scale t of turbulent eddies which can be expressed as;

$$l = \frac{k^3/2}{\epsilon}, \tag{2.12}$$

$$t = \frac{k}{\epsilon} \tag{2.13}$$

Viscosity is a coefficient term which measures momentum transfer between different particles in a fluid and can be expressed as;

$$\nu = lv \tag{2.14}$$

where l and v denote the length scale and the velocity scale.

The turbulent viscosity ν_T can then be expressed as;

$$\nu_T = C_\mu \frac{k^2}{\epsilon} \tag{2.15}$$

where C_μ denotes a dimensionless constant equal to 0.09.

The transport equations for k and ϵ then become;

$$\frac{\partial k}{\partial t} + U_j \frac{\partial k}{\partial x_j} = 2\nu_T \overline{S}_{ij} \overline{S}_{ij} + \frac{\partial}{\partial x_j}[(\nu + \frac{\nu_T}{\sigma_k})\frac{\partial k}{\partial x_j}] - \epsilon \tag{2.16}$$

$$\frac{\partial \epsilon}{\partial t} + U_j \frac{\partial \epsilon}{\partial x_j} = \frac{\epsilon}{k} c_{\epsilon 1} 2\nu_T \overline{S}_{ij} \overline{S}_{ij} + \frac{\partial}{\partial x_j}[(\nu + \frac{\nu_T}{\sigma_\epsilon})\frac{\partial \epsilon}{\partial x_j}] - c_{\epsilon 2}\frac{\epsilon^2}{k} \tag{2.17}$$

where C_μ, σ_k, σ_ϵ, $C_{\epsilon 1}$ and $C_{\epsilon 2}$ are all model constants.

There are other EVM models like the $k-\omega$ and the $k-\omega$ SST model which are similar to the $k-\epsilon$ model where the difference is made by replacing the specific dissipation rate ω instead.

2.3.1.3 Reynolds Stress Transport Models (RSM)

The RSM model also known as the second-moment closure model solves the transport equation for each component of the Reynolds stress tensor. The components of the stress tensor are calculated directly by solving its transport equation.

The transport equation for the Reynolds stresses can be obtained by multiplying the instantaneous Navier-Stokes equations with the Reynolds stresses and then time-averaging.

$$\begin{aligned} \frac{\partial \overline{u_i' u_j'}}{\partial t} + \frac{\partial \overline{u_i' u_j'}}{\partial x_k} U_k = -\overline{u_j' u_k'}\frac{\partial U_i}{\partial x_k} - \overline{u_i' u_k'}\frac{\partial U_j}{\partial x_k} \\ -\frac{\partial}{\partial x_k}(\overline{u_i' u_j' u_k'} + \frac{1}{\rho}\delta_{ik}\overline{u_j' p'} + \frac{1}{\rho}\delta_{jk}\overline{u_i' p'} - \nu\frac{\partial \overline{u_i' u_j'}}{\partial x_k}) \\ +\overline{\frac{1}{\rho}p'(\frac{\partial u_i'}{\partial x_j} + \frac{\partial u_j'}{\partial u_j'})} - 2\nu\overline{\frac{\partial u_i' \partial u_j'}{\partial x_k x_k}} \end{aligned} \tag{2.18}$$

The above equation can be rewritten as;

$$\frac{\partial \overline{u_i' u_j'}}{\partial t} + C_{ij} = P_{ij} + D_{ij} + \Pi_{ij} - \varepsilon_{ij} \tag{2.19}$$

where C_{ij}, P_{ij} , D_{ij}, Π_{ij} and ε_{ij} denote the convective term, production term, diffusion term, the pressure-strain term and the turbulence dissipation term respectively. Here the terms which are to be modeled are the turbulent diffusion term, the dissipation term and the most challenging is the pressure-strain strain term. The convective and production term are known so do not need any modeling [6].

2.3.1.4 Large-Eddy Simulation(LES)

The LES turbulence model is the one used in this study and here a brief explanation on the theory behind the model is given.

LES is a scale resolving model. Unlike the RANS approaches it resolves the large scales of turbulence which are the most important and models the small scale fluctuations. In simple words here there is less modeling of turbulence rather than resolving. Figure 2.2 shows the energy spectrum for the turbulent kinetic energy.

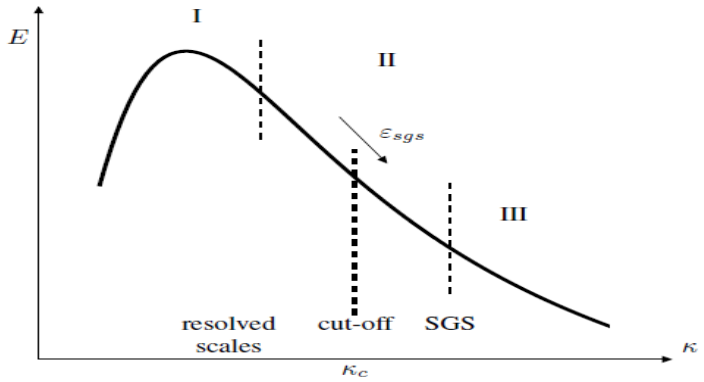

Figure 2.2: Energy Spectrum [5]

Scale resolving depends on the cut-off wavenumber κ_c which depends on the filter length Δ and it is described as $\kappa_c = \pi/\Delta$. Moving the cut-off line to the right improves accuracy as it is approaching DNS. Scale separation depends on the choice of filter used. There are several types of filters like the box or top-hat which is the most common used filter, the Gaussian filter and the sharp cut-off filter.

Contrary to the RANS model any quantity in LES is obtained by a filtering operation rather than the averaging operation as;

$$\phi = \overline{\phi} + \phi^{SGS} \tag{2.20}$$

where ϕ, $\overline{\phi}$ and ϕ^{SGS} represent the desired quantity, the resolved or filtered desired quantity and the sub-grid field respectively.

Taking a case for velocity,

$$u_i(x_j, t) = \overline{u_i}(x_j, t) + u^{SGS}(x_j, t) \tag{2.21}$$

where $u_i(x_j, t)$, $\overline{u_i}(x_j, t)$ and $u^{SGS}(x_j, t)$ are the instantaneous velocity, the filtered velocity and the sub-grid velocity field, respectively.

The filtered velocity can be written as a convolution integral.

$$\overline{u_i}(x_j,t) = \int G_i(r_j,x_j)U_i(x_j+r_j,t)dr_j \tag{2.22}$$

where G is a filter function.

Applying filtering operations to the N-S equations gives filtered N-S equations as,

$$\frac{\partial \overline{u}_i}{\partial x_i} = 0 \tag{2.23}$$

$$\frac{\partial \overline{u}_i}{\partial t} + \frac{\partial}{\partial x_j}\overline{u}_i\overline{u}_j = -\frac{1}{\rho}\frac{\partial \overline{p}}{\partial x_i} + \nu\frac{\partial^2 \overline{u}_i}{\partial x_j x_j} - \frac{\partial \tau_{ij}}{\partial x_j} + \overline{F}_i \tag{2.24}$$

Equations 2.23 and 2.24 denote the continuity and momentum equation respectively. $\overline{F_i}$ is the resolved aerodynamic drag force and τ_{ij} is known as the subgrid stress tensor which can be expressed as;

$$\tau_{ij} = \overline{u_i u_j} - \overline{u}_i\overline{u}_j \tag{2.25}$$

The small scales are to be modeled in LES so a modeling approach needs to be chosen. The Smagorinky Subgrid Scale model is chosen for this study however there are other several modeling approaches that could be used such as, the Dynamic Smagorinky model, the Wall-Adapting Local-Eddy (WALE) subgrid scale model, the Similarity models and several others.

The Smagorinky Model is the simplest subgrid model to model the small scales. Similar to the EVM models, it uses the concept of mixing length hypothesis to model the sub-grid stresses.

The sub-grid stresses τ_{ij} can be modeled as;

$$\tau_{ij} - \frac{1}{3}\tau_{kk}\delta_{ij} = -2\nu_{SGS}\overline{S}_{ij} \tag{2.26}$$

where ν_{SGS} denotes the subgrid viscosity. Through dimensional analysis ν_{SGS} can be expressed as $\nu_{SGS} = lv$ where l and v denote length and velocity scales, respectively. The turbulent length scale can be expressed as $l^2 = (C_s\Delta)^2$ where C_s is the subgrid viscosity coefficient. The subgrid stresses can then be expressed as;

$$\tau_{ij} = -2(C_s\Delta)^2|\overline{S_{ij}}|\overline{S_{ij}} \tag{2.27}$$

where $\nu_{SGS} = (C_s\Delta)^2|\overline{S_{ij}}|$ and $\overline{S_{ij}}$ is the strain rate tensor.

A short-coming of the Smagorinsky model however is that the C_s coefficient is not universal and constant, that it depends on the local flow conditions. In this study C_s is taken to be 0.1. The Smagorinsky model also does not capture the near wall boundaries effect accurately. To account for this the van Driest Damping function is incorporated in the subgrid viscosity equation written as;

$$f_s = 1 - exp(-\frac{y^+}{A^+}) \tag{2.28}$$

where y^+ is the normalized distance from the wall in viscous wall units ($y^+ = yu_\tau/\nu$). u_τ is the shear velocity or friction velocity given by ($u_\tau = \sqrt{\tau_w/\rho}$) where τ_w is the wall shear stress at the wall and A^+ is a non-dimensional constant taken to be approximately 25. The purpose of the van Driest damping function is to reduce the subgrid-scale viscosity near the wall.

To accurately resolve the turbulent structures near the wall the LES method requires a high mesh resolution in the wall boundary layer not only in the direction normal to the wall but also in the flow direction. As a consequence this results in high computational costs.

2.3.1.5 Initialization and Inflow for LES

Inaccurate results in LES often arise due to the numerical setup rather than the turbulence model. Initialization of the the flow is one of the setup procedures which can introduce errors.

One way of initializing the flow is by introducing noise to the mean flow. This approach however suffers from numerical instability in the sense that it produces an uncorrelated velocity field incapable of sustaining growth of coherent turbulent structures. Another approach is by using an initial condition from a similar simulation (precursor simulation by RANS) to start the LES simulation.

However in *STAR-CCM+*, the Synthetic Eddy Method (SEM) is used to initialize the inlet fluctuations and give turbulent eddies across the inflow boundaries. The size of these eddies is the characteristic scale of turbulence e.g length scale. To set the inflow inlet conditions in this study Reynolds stress and turbulent length length scale are specified. A sufficient distance between the inflow boundary and the region of interest must be allowed to for these turbulent structures to develop. This distance varies from case to case for example in channel flow a distance of at least ten half-heights is required [1].

2.3.2 Wall Treatment

The region near the wall is very important as mentioned in the previous section. Here the velocity gradients are the highest as the flow tends to go zero due to the

no-slip condition and also the wall region is a source of vorticity. Thus it is inevitable to try to resolve the wall region accurately. The boundary layer in the near wall region can be divided into two regions; the inner region and the outer region. The inner region can be broken into;

- *Viscous sublayer:* This is the part of the inner layer which is in contact with the wall. Fluid flow here is governed by viscous diffusion. It is found where $y^+ \leq 5$.
- *Logarithmic layer:* This region is dominated mostly by turbulent diffusion. It is found where $y^+ \geq 30$.
- *Buffer layer:* This is the transitional region between the viscous sublayer and the logarithmic layer $5 \leq y^+ \leq 30$.

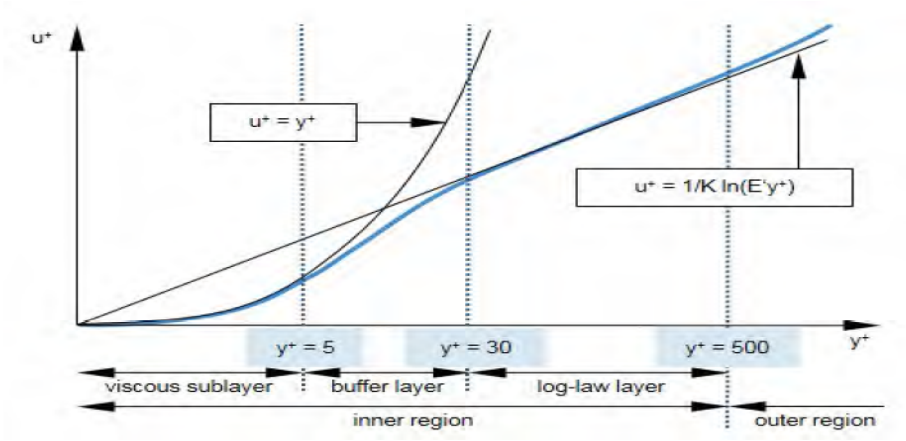

Figure 2.3: The Wall Region [1]

STAR-CCM+ has three types of wall treatment can be chosen; the *low-y+*, the *high y+* and the *all-y+* wall treatment.

- *The low-y+ treatment:* This treatment resolves the viscous sublayer. It requires a sufficiently fine mesh with near-wall cells located at y+ of around unity thus the computational cost is higher with this approach. It is used for low Reynolds number flows.
- *The high-y+ treatment:* This approach resolves the log-law layer assuming that the near-wall cells are located in the log-layer layer ($y^+ > 30$). Unlike the previous approach it requires a less fine mesh.
- *The all-y+ treatment:* This treatment is a hybrid of the low y+ and the high y+ treatment.

2.4 Modeling the Atmospheric Boundary Layer (ABL)

Modeling roughness within the ABL is generally done by moving the logarithmic region of the boundary layer closer to the wall. This can be done by reducing the wall function coefficient E. The preferred method of modeling roughness is to use

the Richard and Hoxey law for the velocity distribution u^+_{RH} [1].

$$u^+_{RH} = \frac{1}{\kappa}\ln(\frac{y_0 + y}{y_0}) \tag{2.29}$$

where y_0, κ and y denote the physical roughness length, the von Karman constant and the normal distance from the wall to the cell centroid, respectively.

Within the ABL the flow is turbulent in nature hence the velocity distribution in the overlap or logarithmic region of the boundary layer is provided by the law of the wall which states that the average velocity of a turbulent flow at a certain point is proportional to the logarithm of the distance from that point to the wall given by;

$$u^+ = \frac{1}{\kappa}\ln(E'y^+) \tag{2.30}$$

where $E^{'}$ is the modified wall function coefficient defined by $E^{'} = E/f$. E is the wall function coefficient and f is the roughness function which is unity for smooth walls. u^+ is the non-dimensional velocity given by $u^+ = u/u_\tau$ where u is the actual velocity. The default values of E and κ are 9.0 and 0.42, respectively in *STAR-CCM+*. The roughness function f is a function of the roughness parameter R^+ which is expressed as;

$$R^+ = \frac{ru_\tau}{\nu} \tag{2.31}$$

where r is the equivalent sand-grain roughness height. r maybe obtained from literature or empirically for the specified model. For rough walls the roughness function is then given by;

$$f = \begin{cases} 1 & \text{for } \mathrm{R}^+ \leq R^+_{smooth} \\ \left[B(\dfrac{R^+ - R^+_{smooth}}{R^+_{rough} - R^+_{smooth}}) + CR^+\right]^a & \text{for } \mathrm{R}^+_{smooth} < R^+ < R^+_{rough} \\ B + CR^+ & \text{for } \mathrm{R}^+ > R^+_{rough} \end{cases} \tag{2.32}$$

where the exponent a is expressed as:

$$a = sin\left[\frac{\pi}{2}\frac{log(R^+/R^+_{smooth})}{log(R^+_{rough}/R^+_{smooth})}\right] \tag{2.33}$$

The default values in *STAR-CCM+* are B=0, C = 0.253, R^+_{smooth} =2.25 and R^+_{rough}= 90. To give physical results ($u^+ > 0$) then $y >> y_0$.

However direct modeling of the ABL with LES in *STAR-CCM+* is not possible due to the absence of surface roughness model. It is with the RANS and DES models that are capable of modeling roughness [1].

2.5 Forest Modeling

Heterogeneous forest is the type of forest characterized with different canopy distribution. Thus it differs from the homogeneous forest which has uniform distribution. This is indicated with the Plant Area Density (PAD) which is the total plant area per unit volume. The canopy distribution influences the flow physics and turbulent characteristic in the ABL. For example the momentum is not only absorbed by the ground but all through the depth of the of the canopy as the aerodynamic drag. It is given as,

$$F_i = -C_D(PAD)\rho|U|u_i \tag{2.34}$$

where C_D, PAD and U denote the forest drag value set to 0.15, the Plant area density and the local velocity magnitude respectively [18]. Leaf Area Density (LAD) is the one-sided leaf area per unit volume. LAD describes the vertical canopy structure in each horizontal layer. When the whole plant is considered (branches, stems, roots) then the canopy structure is described by PAD [9]. In modeling the heterogeneous forest, PAD is used while LAD is used to model homogeneous forest.

High turbulent intensities are encountered within the canopy making it difficult to characterize the flow [13].

2.6 Numerical Methods

Fluid motion are described with mathematical models like partial differential equations. These equations can rarely be solved analytically except in special cases. As mentioned earlier CFD technique can be used to model the flow motion numerically. Therefore, numerical *discretization schemes* which approximate the differential equations by a system of algebraic equations can be employed. This approximations are applied to a small domain the so-called cell in *STAR-CCM+* so that the numerical solution provides results at discrete locations in space and time. A numerical grid is setup which is the discrete representation of geometrical domain where different quantities can be computed within the grid.

2.6.1 Properties of Numerical Solution Methods

The numerical solution should have certain features. The most important ones will be discussed in this section.

2.6.1.1 Consistency

As the grid spacing reduces or tends to zero the solution should be exact. The difference between the approximated discretized solution and the exact solution is the truncation error. This is the remainder between the approximated solution and the

exact solution. The approximations are usually given by Taylor Series Expansion at a grid point. For a numerical method to be consistent the error should become zero as the grid spacing $\Delta x_i \to 0$ and the time step $\Delta t \to 0$. The truncation error is proportional to the power of the grid spacing Δx_i^n and the time step Δt^n. For consistency $n > 0$. If the most important term is proportional to $\Delta(x_i)^n$ or Δt^n then we say that the method is of n^{th} approximation [6].

2.6.1.2 Stability

A numerical solution is said to be stable if the error propagation converges. This means that the error doesn't not get amplified during the simulation. When non-linearities along with boundary conditions exist then stability becomes hard to investigate thus it is more common to investigate stability for linear problems with constant coefficients without boundary conditions. The von Neumann's method is the most common way to investigate stability [6].

2.6.1.3 Convergence

As the grid spacing tends to zero, a numerical solution is said to be convergent if the the solution of the discretized equations tends to the exact solution of the differential equation. For linear initial value problems, the Lax equivalence theorem states that "given a properly posed linear initial value problem and finite difference approximation to it that satisfies the consistency condition, stability is a necessary and sufficient condition for convergence" [6].

For non-linear equations it is more difficult to check for convergence. If a method is consistent and stable we find that the solution converges to a grid-independent solution. For sufficiently small grid sizes, the rate of convergence is governed by the order of principal truncation error component [6].

2.6.1.4 Conservation

The numerical scheme should adhere to the conservation laws of the governing equations. It is an important property which imposes a constraint on the solution error. If the conservation laws are insured, the error can only improperly distribute these quantities over the solution domain. Errors due non-conservation are observed mostly in relatively coarse grids [6].

2.6.1.5 Boundedness

Numerical solution should lie within proper bounds. Quantities like density and kinetic energy which are physically non-negative must always have a positive value and other quantities like concentration must lie between 0% and 100%. First order schemes guarantee boundedness. Unboundedness often arises when the grids are too

coarse [6].

2.6.1.6 Realizability

Models should be setup in a way that physically realistic solutions are observed. This is not entirely dependent on the numerics but models which are not realizable may result into unphysical solutions and causes the diverged numerical solution [6].

2.6.1.7 Accuracy

Numerical solutions are only approximate solutions. Errors might arise during the development of the solution algorithm but generally speaking errors in numerical simulation can be divided into three categories.

- *Modeling errors*; these errors arise in the setting up of the mathematical model of the fluid flow problem. For example employing a turbulence model where it can't be used is an example of a case which can bring such an error. Assumptions made also contribute to these kind of errors [6].
- *Disretization errors*; The numerical schemes use approximations so it is obvious that there will be an error that are due to the difference between the exact solutions of the conservation equations and exact solutions of the algebraic equations obtained after discretization [6].
- *Iteration errors*; This is the error obtained at each iteration of the numerical simulation [6].

2.6.2 Discretization Schemes

The quality of the numerical solution depends on the discretization scheme used. There are several solution schemes but it is desired to use the one in which the desired accuracy is obtained with the least effort with the available resources. The most common schemes are the Finite Difference (FD), Finite Volume (FV) and the Finite Element (FE) and they are briefly explained here.

2.6.2.1 Finite Difference (FD)

This is the oldest discretization method of differential equations where differential form of the conservation equations. A numerical grid is the solution domain where the solution is calculated at the grid points. At each grid point the differential equations are approximated by Taylor series expansion. Each node will thus have one discretized equation. FD can be applied to essentially any type of grid, structured or unstructured however it has been mostly applied to structured grids. It is very simple and effective and higher order of accuracy can be obtained especially on fine grids. However conservation is not enforced on this method [6].

2.6.2.2 Finite Volume (FV)

In this study the FV method is used. It is widely used in many CFD tools. The basis of this method starts with the integral form of the governing equations. Instead of solving for the desired quantity on a grid point the FV method solves for the value of the quantity in a cell volume. Thus the solution domain is divided into a finite number of control volumes which make the cells of the computational grid. The values are computed at the cell centre. In the end a set of linear algebraic equations is obtained with the total number of unknowns corresponding to the number of cells in the computational grid. FV can be applied to both structured and unstructured grids. It is perhaps the simplest to understand and to program and maybe this is the reason that it commonly used. In 3D it becomes more difficult to implement the FV method compared to the FD method [6].

2.6.2.3 Finite Element (FE)

This method resembles the FV method in a number of ways. Just like the FV method the solution domain is partitioned into a set of small discrete volumes or finite elements which are usually unstructured. Unlike the FV method the equations are multiplied by weight/test function before being integrated over the domain.

FE is advantageous when it comes to complex geometries and are relatively easier to analyze mathematically. Since it uses unstructured grids it becomes difficult to find efficient solution methods with the FE method [6].

2.7 Wind Energy

Wind turbines work on the principle of converting incoming wind's kinetic energy into electrical energy. How does this come about is the sole purpose of this section. In addition this section aims to explain the concept of wind turbine aerodynamics as well as give an insight to the forces that a wind turbine system is subjected to.

2.7.1 Wind Turbine Structure

Wind Turbines can be classified according to their functionality on how they generate power or according to their design and configuration. The rotor can generate power either by using the drag component of the incoming wind and these are the so called drag-type rotors or by using the aerodynamic lift. Classification according to design is the most common type of classification. Basically the most apparent way is the positioning of the axis of rotation i.e rotors with vertical axis of rotation, Vertical Axis Wind Turbine (VAWT) and rotors with horizontal axis of rotation, Horizontal Axis Wind Turbine (HAWT).

VAWTs present a number of disadvantages such as low tip-speed ratio, lower power coefficient, not being able to to control power output or speed in case of high speed winds and high production costs. Contrary to VAWTs, HAWTs have the advantages of being able to optimize the rotor blade and speed and power output control capability [8].

It was realized by Albert Betz based on the momentum theory that only a certain portion of the wind's kinetic energy can be extracted and provide useful work. He realized that this optimal value is influenced by the ratio of flow velocity of air in front of the rotor disc to the velocity of flow velocity behind the rotor disc. This is the Betz limit power coefficient $C_{p,max}$. The value was found to be 0.593 [8]. It was derived on the assumption that the rotor disc is ideal meaning that the flow is friction-less, incompressible and there is no rotational component of velocity in the wake and without considering the design of the rotor disc . However in the real case the power coefficient C_p will always be smaller than this value. Modern wind turbines however are optimized to operate close to 0.5. Drag-type rotors achieve a maximum power coefficient $C_{p,max}$ of 0.2. Their counter parts lift-based rotors achieve higher coefficients of power and hence they have been widely used.

The basic components of a wind turbine are the rotor which captures the incoming wind and converts it into electrical energy and the hub which is part of the rotor connects the the rotor blades to the rotor shaft. The hub may contain the Blade Pitch Control system for power and speed control, however smaller wind turbines might lack this. The hub, the blade pitch mechanism system and the rotor shaft form the low-speed shaft. The low-speed shaft isn't directly coupled to a generator due to the noise and mechanical strength. It is connected to the gearbox which achieves a high speed ratio. The gearbox and the generator shaft are part of the high-speed shaft. The nacelle is the housing of these components. A yaw system is also put in place to make sure the rotor and the nacelle are facing towards the direction of the incoming wind. The nacelle is mounted on a tower which goes to the base (foundation). The hub height is important design parameter as the higher the hub, the higher the wind speed. The rotor disc area is crucial since it determines the amount of wind energy which can be captured by a wind turbine. Figure 2.4 shows a schematic of a HAWT and its components.

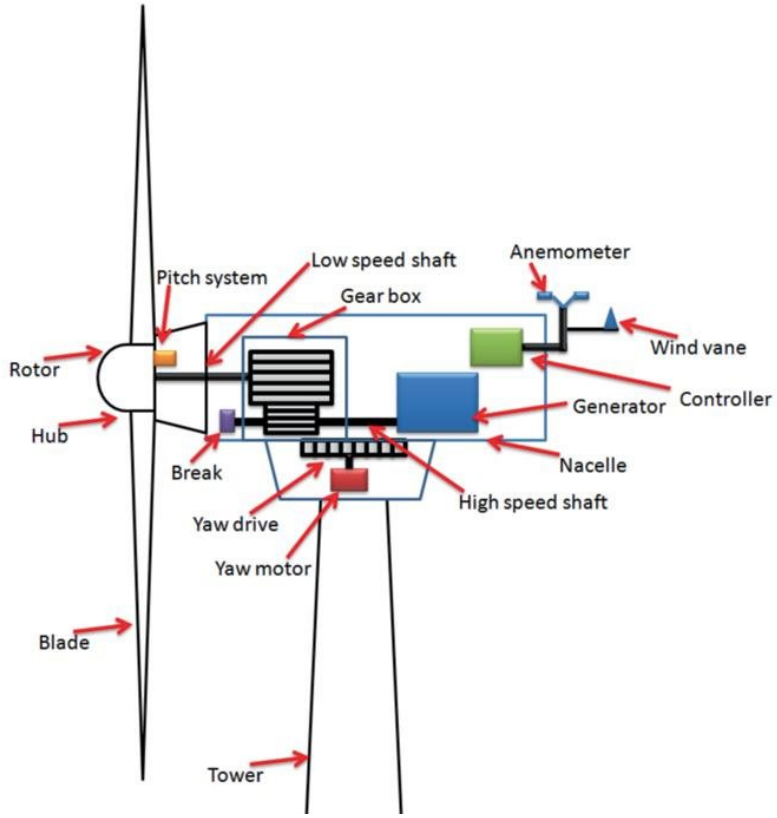

Figure 2.4: Horizontal Axis Wind Turbine [15]

2.7.2 Wind Turbine Aerodynamics

The rotor blades cross-section has an airfoil shape. The forces acting on on a rotor blade can be calculated using the Blade Element Momentum Theory (BEMT). However before describing the BEMT it is better to look at the aerodynamic make up of an airfoil. Looking at a single element of the rotor blade can make analysis easier. (See Fig. 2.5)

The incoming wind or axial wind is not the actual wind observed by the blade section but rather the relative velocity v_r which is the vector resultant of the incoming wind v_w and the blade tangential velocity u. The two forces acting on the blade are the Lift force and the Drag force. The former is perpendicular to v_r while the latter is parallel to v_r. From the resultant of the lift and drag forces the thrust and torque are obtained. The axial velocity is aligned with the thrust which causes bending of the blades backwards and this should be minimized as much as possible. The Torque is in the direction of the blade tangential velocity u which causes rotation. It is given by the product of the distance between the blade element and the axis of rotation r and the angular velocity of the blade ω. The angle of attack α is defined as the angle between the airfoil chord and the relative velocity observed by the blade v_r. The blade pitch angle ϑ (including the blade twist angle) is the angle formed between the rotor plane and the chord.

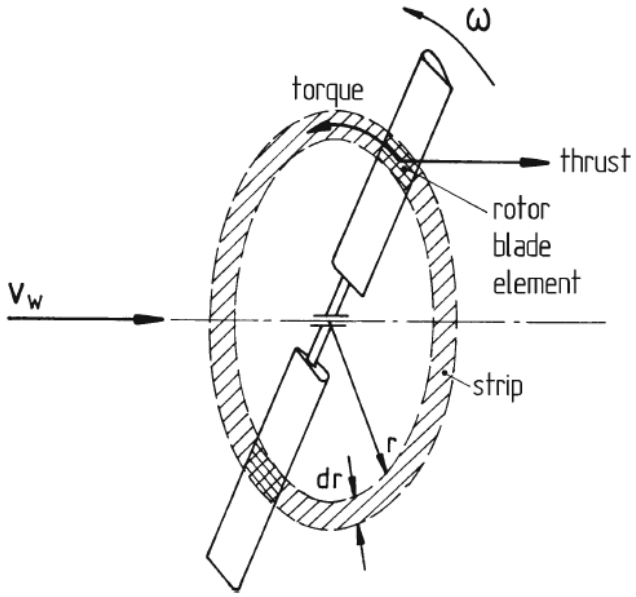

Figure 2.5: Wind Turbine Rotor with incoming flow [8]

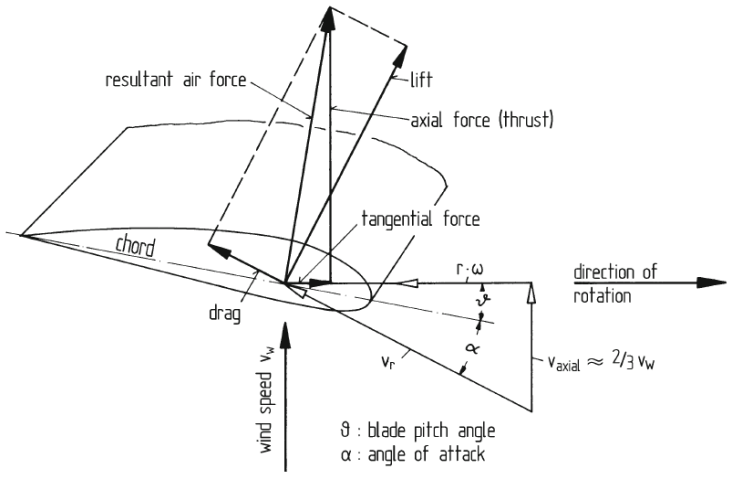

Figure 2.6: Schematic of Blade Element Theory of an airfoil subjected to aerodynamic forces [8]

2.7.2.1 Blade Element Momentum Theory (BEMT)

The Blade Element Momentum Theory (BEMT) combines the theory from the momentum theory and the Blade Element Theory (BET) to compute the forces acting on a rotor blade.

The momentum theory models the rotor as an infinitesimally thin disc with a pressure difference across the rotor disc. In other words the rotor is made up of infinite number of blades with zero thickness. Due to the pressure difference thrust is generated over the rotor. The Blade Element Theory breaks down the rotor blade into several small parts called blade elements and determines forces on each of the blades.

The total force is obtained by integrating the forces along the entire length of the blade and averaging the result over one rotor revolution. The important assumption taken into account in the BET is that there is no interaction between different blades elements [8] [16].

The thrust and torque acting on one blade can then be given by;

$$dF_x = \sigma' \pi \rho \frac{V_r^2 (1-a)^2}{cos^2 \beta} \Big(C_L sin\beta + C_D cos\beta \Big) r dr \tag{2.35}$$

$$dT = \sigma' \pi \rho \frac{V_r^2 (1-a)^2}{cos^2 \beta} \Big(C_L cos\beta - C_D sin\beta \Big) r dr \tag{2.36}$$

where β, C_L, C_D, a and σ' are the angle between the relative velocity observed by the rotor blade and the axial velocity of the blade, the lift coefficient, drag coefficient, the axial induction factor and the local solidity. Total thrust and torque can be obtained by integrating the equations over the entire span of the blade. [10]

2.7.3 Blade Pitch Control

Power and speed control is necessary for wind turbines as at high speeds the captured wind power might exceed the rated power of the wind turbine. This may damage the wind turbine and hence a control function has to be put in place to limit the rotational speed and power and make sure that the wind turbine operates within the desired range and as well as to optimize the power output at lower wind speeds.

Power and speed control can be achieved by adjusting the angle of attack, the rotor swept area and the effective free-stream velocity at the rotor blades. The most effective way of having speed and power control is by adjusting the Blade Pitch angle.

Blade Pitch Control can be achieved in two ways; adjusting the the blade pitch hence the angle of attack to smaller values so that the power input decreases and the other way is to increase the angle of attack to a maximum value called the critical angle of attack where by the flow separates and thus limit the power input. This condition is known as stall and hence stall control. Stall Control can be passive or active. The former being that being a self-regulating mechanism in the sense that without changing the blade pitch angle stall will occur with increasing wind speeds past the limit set by a wind turbine while the latter involves adjusting the blade pitch angle at different wind speeds.

The control methods mentioned above were assumed to be of approximately constant rotation. However most of the wind turbines nowadays are integrated with both Blade Pitch Control and Variable-Speed Regulation. With the variable speed option it means that for the rotor could be operated at the optimum rotational speed for each wind speed and thus the maximum available power is captured.

2.7.4 5-MW Reference Wind Turbine

The structural dynamic response of the wind turbines is assessed using the NREL offshore 5MW Baseline Wind Turbine. It is a conventional three-bladed upwind variable-speed blade-pitch-to feather-controlled turbine. This model has been used widely as a benchmark turbine in wind energy research community. Table 2.1 shows its important properties.

Table 2.1: Properties of the 5-MW NREL Reference Wind Turbine Model

Rating	5 MW
Rotor Orientation, Configuration	Upwind, 3 Blades
Control	Variable Speed, Collective Pitch
Rotor, Hub Diameter	126 m, 3 m
Hub Height	90 m
Cut-In, Rated,Cut-Out Wind speed	3m/s, 11.4m/s, 25 m/s
Cut-In, Rated Rotor Speed	6.9 rpm, 12.1 rpm
Rotor mass	110,000 kg
Nacelle mass	240,000 kg
Tower mass	347,460 kg

The operation of the wind turbine model under steady-state conditions are presented in Fig. 2.7. One can observe that the rotor speed and generator speed both increase with wind speed. The rotor torque and power vary quadratically and cubically in region 2 with the wind speed. Above the rated speed they are kept constant by active blade-pitch control. Maximum out-of-plane tip deflection is reached at the rated speed which corresponds to maximum thrust. As seen from the Fig. 2.7 the operating range is between 3m/s to 25m/s. Below this limit the wind turbine will not generate any power (cut-in) and above this point the wind is too strong for the wind turbine to operate and so it will stop power generation (cut-off). Above the rated speed of 11.4m/s the blade pitch control holds the rotor speed at a constant value as shown by the red line in Fig. 2.7.

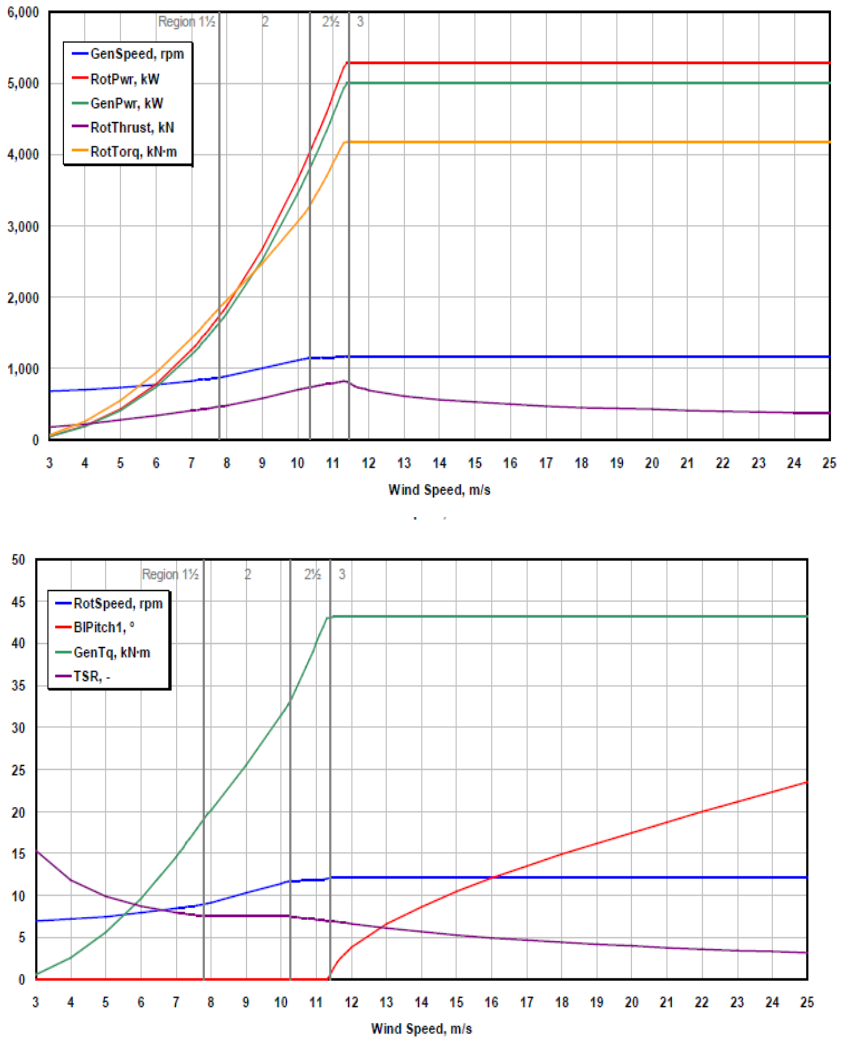

Figure 2.7: Steady-state operating condition responses for the NREL offshore 5-MW Baseline Wind Turbine. [11]

3
Methodology

This section explains the method used and the setup procedures employed in this work. Two cases are simulated; homogeneous and heterogeneous forests.

First the LES simulations are carried out using the CFD software *STAR-CCM+*. The computed airflow is then supplied to an aero-elastic solver *FAST* to assess the structural dynamic response of 5MW-NREL turbine. This is done by extracting the instantaneous velocity data from the CFD simulations and converting them into binary files which are then read by FAST solver from NREL. The reasons for using the wind turbine model are explained in section 2.7.4 and also due to unavailability of data for the 2MW wind turbines in the Röbergskullen wind farm.

The simulated wind is blowing from 216° with respect to the North has a speed of 10m/s.

3.1 Computational Domain

The generated computational domain is a complex terrain obtained from airborne Laser data (LAS data) which represent the real topography of Röbergskullen wind farm. The domain is used for analysis of two cases; homogeneous and heterogeneous forests modeling. The domain size, initial and boundary conditions for both the homogeneous and heterogeneous forest modeling are identical.

The inlet of the domain is set up to be perpendicular to the incoming wind at a direction of 216° with respect to the North.

The domain should be setup in such a way that the flow is going to be fully developed for proper analysis of the flow. Since LES is used this means that the domain should be of the dimension such that the largest scales of turbulence are properly resolved and at the same time fine enough to model the smallest scales. The ultimate goal for grid mesh size is to ensure the grid-independency results [3] .

The coordinate system is such that the x-axis is on the streamwise direction so the incoming wind is parallel to the x-axis. The y-axis is parallel to the vertical direction and the z-axis is parallel to the spanwise direction. These dimensions should be compatible with the largest turbulent structures in order to properly analyze the

flow. The computational domain height (H) in this study is considered about 1000m with respect to the lowest ground elevation.

The width of the domain (W) should be chosen so that the turbulent structures to freely move without being suppressed. W is chosen to be 4000m in this study. It is desired to have a square base area but this only results into more computational cells and longer simulation time requiring massive hardware resources. It is seen that to achieve desirable results the width of the domain should be four times larger than the height (W=4H) [3].

The length of the domain (L) is 6000m which is six times greater than the height of the domain. According to the study by Bechmann [3], it was seen that the appropriate domain size follows $6H \times 4H \times 1H$ ratio for the length, width and height, respectively. Eight wind turbines are investigated in this study. The met mast is located close to the center of the domain. The locations of the met mast and the

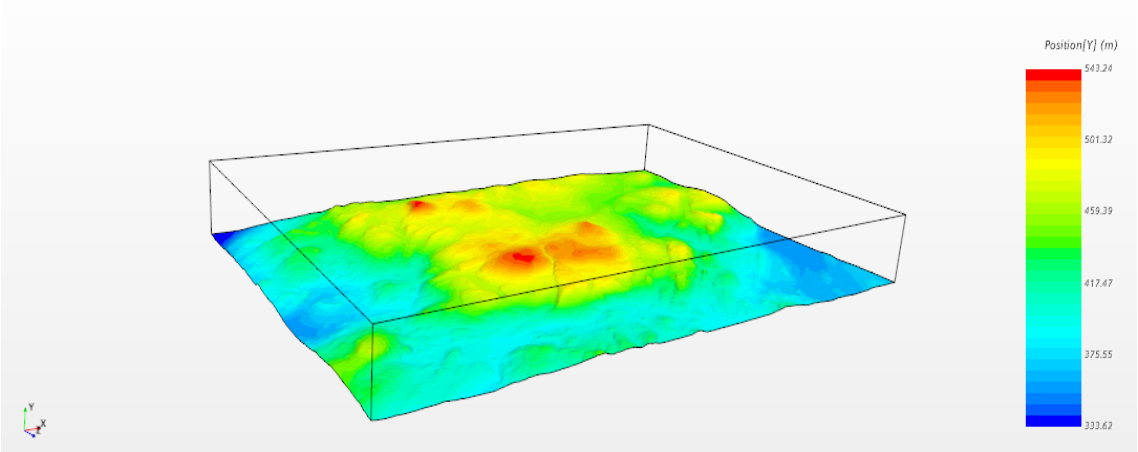

Figure 3.1: The Computational Domain

eight wind turbines used in the computational domain are shown in Table 3.1. They are given in the Swedish Reference Frame (SWEREF 99 Coordinate system).

Table 3.1: Locations of Met mast and wind turbines in the domain

	SWEREF 99	**CFD Domain(x,z) [m]**
Centre of domain	N 6682821.00, E 457085.00	(0,0) height
Met mast	N 6683430.11, E 457058.24	(477,-379)
Wind turbine 1	N 6683515.63, E 457022.21	(525,-459)
Wind turbine 2	N 6683211.26, E 457226.85	(399,-115)
Wind turbine 3	N 6683002.67, E 456844.56	(6,-301)
Wind turbine 4	N 6682839.94, E 457434.30	(221,271)
Wind turbine 5	N 6682634.43, E 456895.03	(-263,-44)
Wind turbine 6	N 6682554.50, E 457224.88	(-133,270)
Wind turbine 7	N 6682403.92, E 456355.07	(-776,-345)
Wind turbine 8	N 6682151.38, E 456874.95	(-665,223)

Because of the complex topography of the studied wind farm, each wind turbine has its own elevation given in Table 3.2.

Table 3.2: Elevations from the ground of each individual wind turbine

	Elevation Y (m)
WT1	528
WT2	509
WT3	508
WT4	521
WT5	524
WT6	526
WT7	511
WT8	532

3.2 Topography and Plant Area Density (PAD)

LAS data for Röbergskullen wind farm have been imported into *STAR-CCM+* as the Stereolithography (STL) file.

Generally the forest is modeled as a drag force in the momentum equation and so it is employed as a momentum source option in *STAR-CCM+*. For the heterogeneous forest modeling the PAD, forest heights and ground heights are also obtained from the LAS data. The PAD defines the varying forest profile in the heterogeneous forest (See section 2.5). The forest height and PAD are provided as inputs in the simulation. For the homogeneous forest with constant Leaf Area Density (LAD), the forest height h_f is assumed to be 20m whereas for the heterogeneous case the PAD and forest height vary at different locations. For the heterogeneous forest the maximum tree height is 38m with average trees height of 20m. The LAD profile for the homogeneous forest is shown in Fig.3.2.

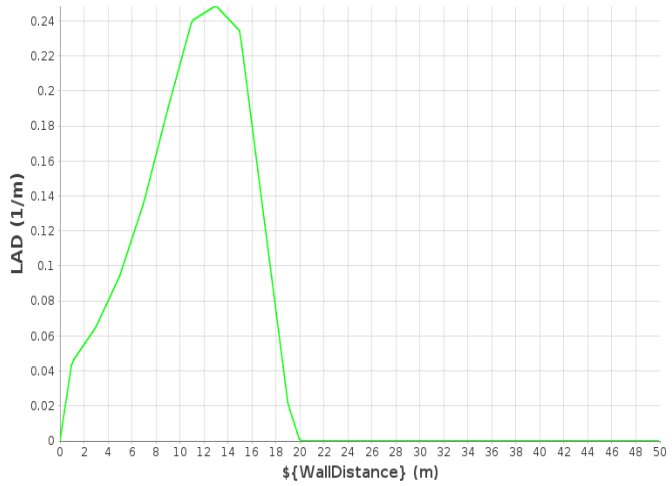

Figure 3.2: Homogeneous forest LAD profile

3.3 Mesh

Identical mesh types are used for both the heterogeneous and homogeneous forest. The *trimmer*, *surface remesher* and the *extruder* mesher are selected. The mesh base size is 15m. The region close to the ground needs special refinement in order to capture the high velocity gradient. The cells here need to be refined to capture the velocity gradients well. The extruder mesher is used instead of the prism layer to resolve the ground region well. The ground is extruded 200m downwards. The vertical grid spacing for the extruded height is chosen to be 2m which is decided based on the roughness length (needs to be greater than the roughness height y_0 to yield physical results). In *STAR-CCM+*, LES method has no roughness model, however the roughness height y_0 is assumed to be 0.02m ($y_0 = 0.001h_f$) [18]. After the extrusion height the vertical grid spacing is 15m. The horizontal resolution is constant everywhere equal 15×15 m^2. This leads to a computational grid with 10.3×10^6 cells.

3.4 LES Simulation Setup

This section gives details on how the LES model is employed. The small scale motions are modeled using the Smagorinsky Subgrid Scale model. The simulation is in 3D performed under constant density, viscosity and temperature conditions taken at standard conditions. The all y+ treatment is used for wall treatment. The initial conditions together with the fluid properties are listed in table 3.3.

Table 3.3: Initial conditions and fluid properties

Type	Quantity	Value
Initial Condition	velocity	[0, 0, 0] m/s
	pressure	0 Pa
Fluid Properties	dynamic viscosity μ	1.85508E-5 Pa.s
	density ρ	1.18415 $\frac{kg}{m^3}$

The coefficients for the *Smagorinsky Subgrid Scale* model are given in the table 3.4.

Table 3.4: Coefficients

Coefficient	Value
Smagorinsky Constant C_s	0.1
von Karman Constant κ	0.41
Damping Coefficient A	25

The boundary conditions are then defined. As depicted in Fig. 3.1, the domain has 6 sides; inlet, outlet, top, bottom and two lateral sides. The inlet is defined as a velocity inlet boundary where streamwise velocity is given as an input as a function of y (vertical direction). This velocity inlet profile is obtained from previous flat terrain LES simulation [18]. The Reynolds stresses together with turbulent length

scale specified to perturb the flow to provide turbulent fluctuations at the the inlet boundary condition. These are taken from previous flat terrain LES simulations [18]. The inlet boundary conditions are chosen such that the simulation results and measurement data at met mast locations from on-site measurement are equal to each other. The length scale is assumed to be 120m which is taken to be approximately the diameter of the rotor disk. The outlet boundary is defined as a pressure outlet with a value of 0 Pa. The bottom surface is the ground and is defined as a wall boundary type, with no-slip condition. The top and the two lateral sides are defined as symmetry planes.

Table 3.5 gives a summary of the boundary conditions set in this LES simulation,

Table 3.5: Boundary conditions

Boundary	**Type**	**Quantity**
Inlet	Velocity	inlet velocity , length scale, Reynolds stresses
Outlet	Pressure	P = 0 MPa
Ground	Wall	
Top	Symmetry	
Lateral sides	Symmetry	

Presentation grids of 200×200 m^2 are created in *STAR-CCM+* to record the instantaneous velocity data that will be fed into the FAST as input data.

The second-order implicit unsteady model is specified as the temporal discretization scheme. The time step chosen is equal to 0.1s. The choice of time step is governed by the Courant-Friedrichs-Lewy number (CFL) . It is given by;

$$CFL = \frac{u\Delta t}{\Delta x} \tag{3.1}$$

where u is the instantaneous streamwise velocity of the flow, Δt is the time step and Δx is the grid spacing in the streamwise direction. It is the ratio of distance travelled by a fluid parcel to the grid spacing. It is a necessary condition for convergence and for stability purposes. In general for explicit scheme it is required that the CFL number is less than one ($CFL < 1$). This ensures that information from one cell propagates to its immediate neighbors and does not bypass any fluid element [3] [6].

The total simulation time is 6360s and the sampling time is 3660s. 5 inner iterations are defined for every time step.

3.5 Aero-elastic Simulation Setup

Instantaneous velocity field from the CFD computation are then fed into the aero-elastic solver *FAST* for structural dynamic response analysis of the eight wind turbines in the wind farm. The total simulation time of 60 minutes is performed. The time step is chosen to be 6.25ms.

4

Results

In this section results for the heterogeneous and homogeneous forests models are presented. The section first looks at the *STAR-CCM+* LES simulation results then looks at the structural dynamic response of the wind turbines from the *FAST* solver.

4.1 LES Simulation

The first set of results that will be shown are the ones which present the flow description.

The streamwise component mean velocity profile is shown in Fig. 4.1 below.

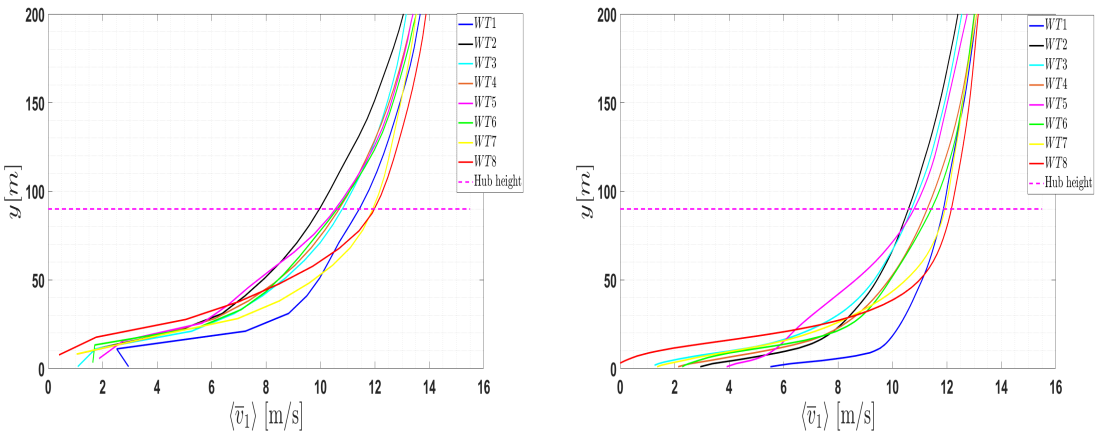

Figure 4.1: Streamwise mean velocity profile of Homogeneous (left) and Heterogeneous (right) forest.

As seen from Fig. 4.1 the mean velocity profile in the heterogeneous forest close to the ground is highly affected by the canopy distribution which varies in the domain. In areas with sparse dense forest density the velocity magnitude is lower compared to the dense areas. The forest acts as a retarder to the flow as explained before. Wind Turbine 1 for example has the highest velocity close to the ground in the heterogeneous forest compared to other wind turbines. Wind turbine 8 in the homogeneous forest, close to the ground, has a higher velocity compared to the same wind turbine in the heterogeneous forest. The influence of the canopy distribution can be shown in Fig. 4.2. As it can be seen the surrounding area of wind turbine

1 has no forest canopies resulting into the highest mean streamwise velocity as discussed above. Also observed in Fig. 4.1 is that the mean streamwise velocity at the hub height have higher magnitudes in the heterogeneous forest compared to the homogeneous forest (higher acceleration in the heterogeneous forest). The vertical

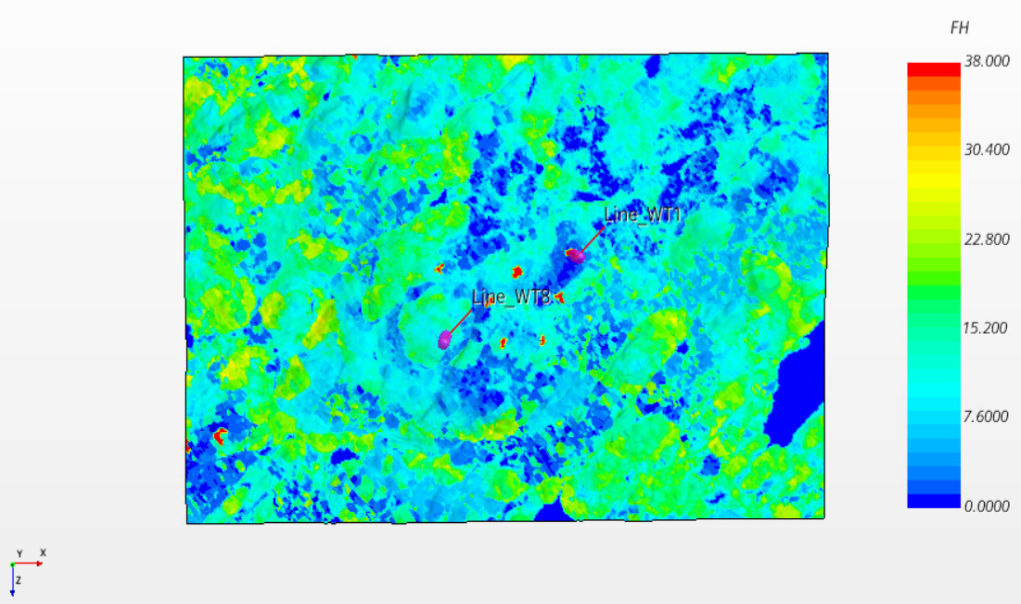

Figure 4.2: Forest Height map of the heterogeneous forest.

direction velocities for the homogeneous and heterogeneous forest modeling are presented in Fig. 4.3. The spanwise velocities for the homogeneous and heterogeneous forest are presented Fig. 4.4. Both vertical and spanwise mean velocity profiles fluctuate around zero as expected (fully developed condition).

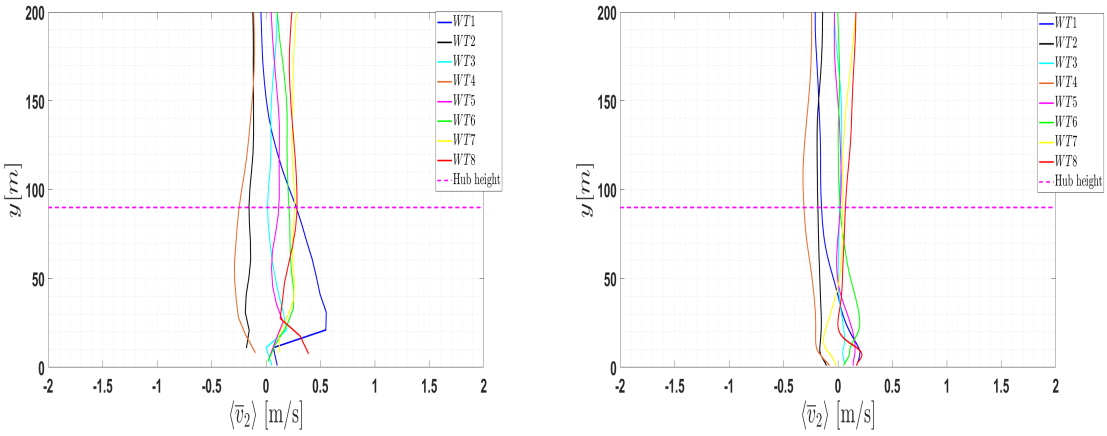

Figure 4.3: Vertical mean velocity profile of Homogeneous (left) and Heterogeneous (right) forest.

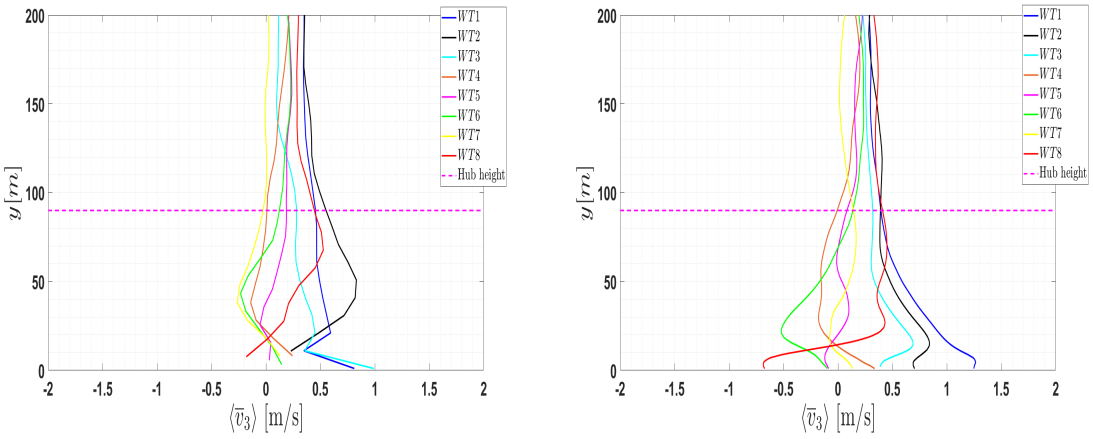

Figure 4.4: Spanwise mean velocity profile of Homogeneous (left) and Heterogeneous (right) forest.

Figure 4.5 displays the turbulent kinetic energy (TKE) along the y direction . It is observed that the turbulent kinetic energy of the homogeneous forest is higher than that of heterogeneous forest. This is because of higher velocity gradients and Reynolds stresses near the ground region in the homogeneous forest [5]. The normal

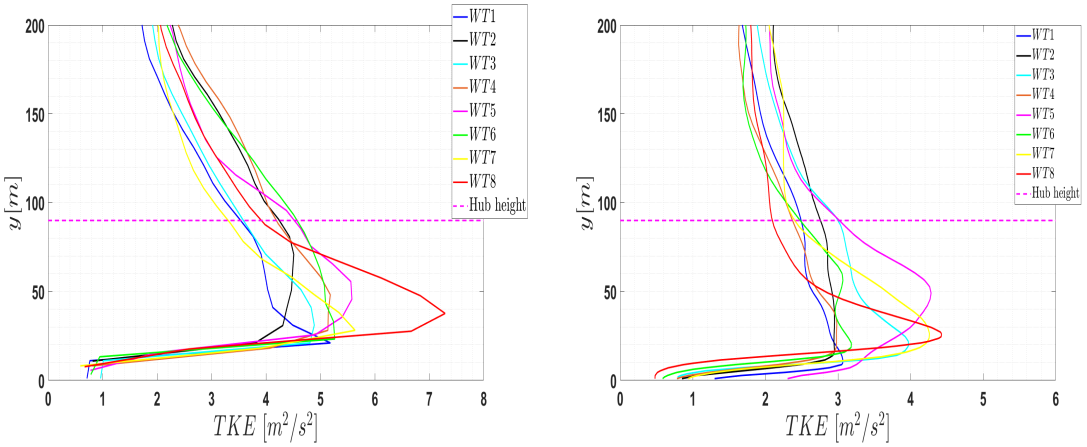

Figure 4.5: TKE profile of Homogeneous (left) and Heterogeneous (right) forest.

Reynolds stresses are then plotted in Fig. 4.6, 4.7 and 4.8.

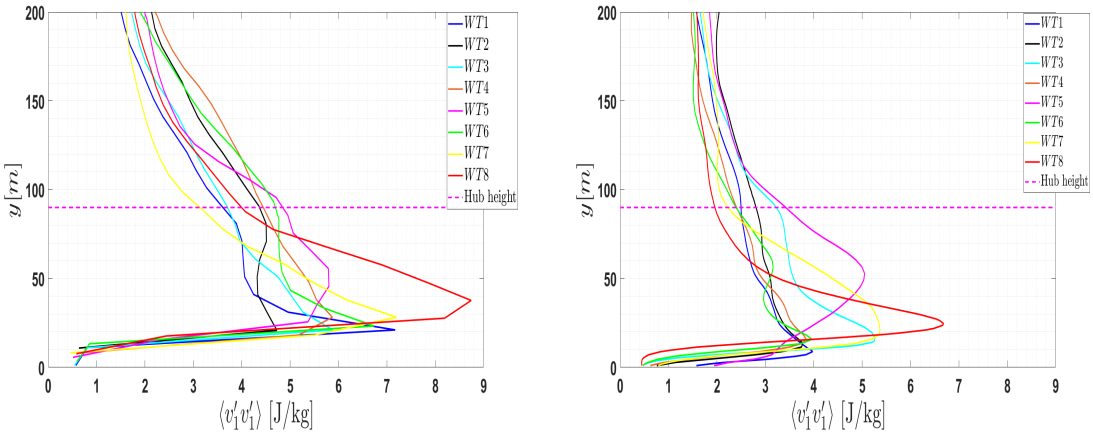

Figure 4.6: Normal Reynolds stresses $< \overline{u}'\overline{u}' >$ in the streamwise direction of Homogeneous (left) and Heterogeneous (right) forest.

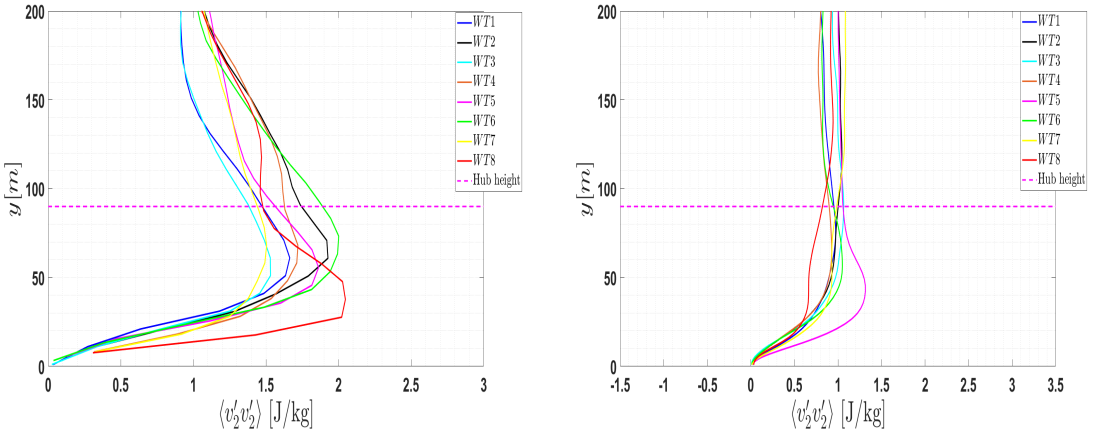

Figure 4.7: Normal Reynolds stresses $< \overline{v}'\overline{v}' >$ in the vertical direction of Homogeneous (left) and Heterogeneous (right) forest

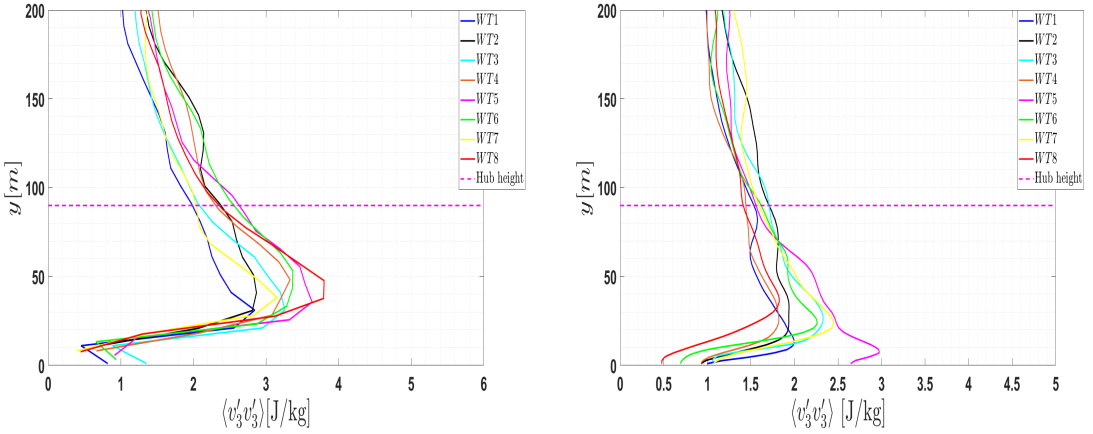

Figure 4.8: Normal Reynolds stresses $< \overline{w}'\overline{w}' >$ in the spanwise direction of Homogeneous (left) and Heterogeneous (right) forest

As seen, the streamwise component of the normal stresses $< \overline{u}'\overline{u}' >$ is the largest component whereas the vertical component $< \overline{v}'\overline{v}' >$ is the smallest as expected. The former is the largest because of the mean flow direction and the latter is the smallest due to the fact that turbulent fluctuations are dampened by the wall [5]. It is also observed that the homogeneous forest has higher normal stresses magnitude compared to the heterogeneous forest. This maybe explained due to the dispersion of forest canopies in homogeneous forest.

The shear Reynolds stresses $< \overline{u}'\overline{v}' >$, $< \overline{u}'\overline{w}' >$ and $< \overline{v}'\overline{w}' >$ are then plotted against the y direction in Fig. 4.9, 4.10 and 4.11. At the wall the viscous stresses are the highest and the shear Reynolds stresses are zero. As the height increases the viscous stresses decrease while the shear Reynolds stresses increase. $< \overline{u}'\overline{v}' >$ is expected to be negative while $< \overline{u}'\overline{w}' >$ and $< \overline{v}'\overline{w}' >$ are almost zero.

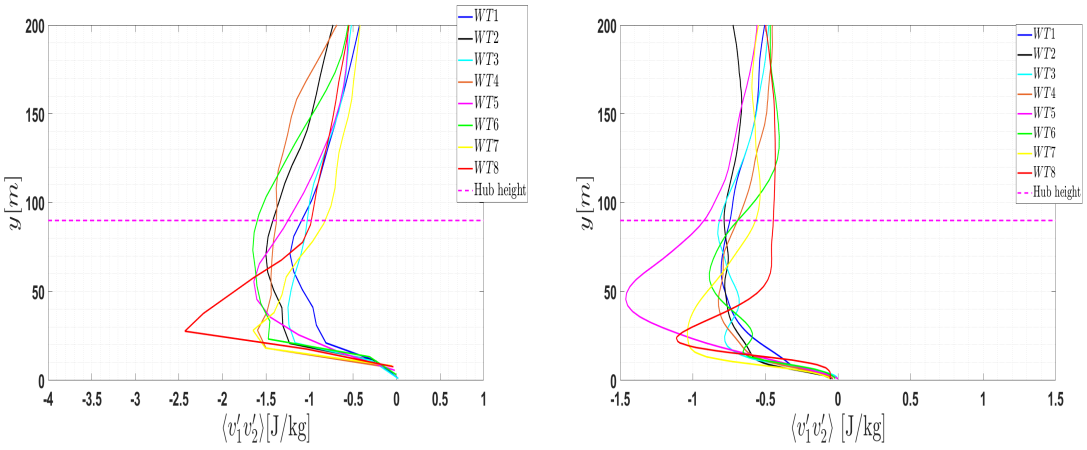

Figure 4.9: Shear Reynolds stresses $< \overline{u}'\overline{v}' >$ of Homogeneous (left) and Heterogeneous (right) forest

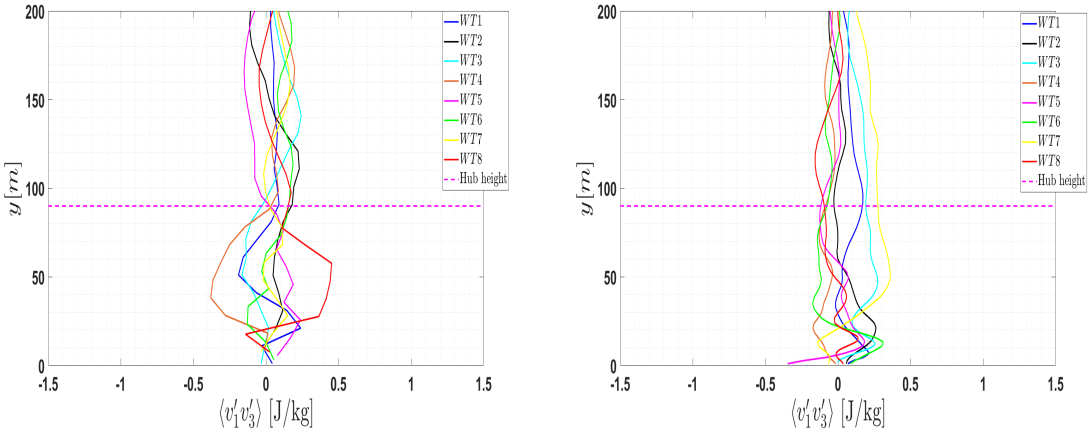

Figure 4.10: Shear Reynolds stresses $< \overline{u}'\overline{w}' >$ of Homogeneous (left) and Heterogeneous (right) forest

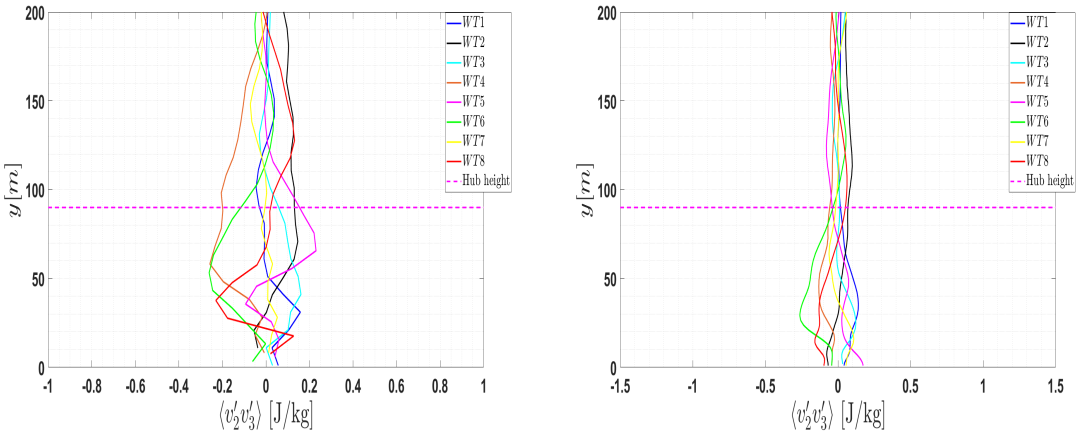

Figure 4.11: Shear Reynolds stresses $< \overline{v}'\overline{w}' >$ of Homogeneous (left) and Heterogeneous (right) forest

4.2 Wind Turbine Structural Dynamic Response

This section presents the results obtained from the aero-elastic solver *FAST* to analyze the structural dynamic response of the wind turbines.

Several output signals are obtained from the solver. These are the *mean* and the *standard deviation (SD)* values of the velocity in all the three directions at the hub height, the *blade-pitch angle*, the *generated rotor torque*, the tower top *rolling moment (Mx)*, *pitching moment (My)* and the *yawing moments (Mz)*. Worth mentioning are the elevations of the wind turbines from the ground shown in Table 3.2. The elevation has an important effect on the streamwise mean velocity on the basis of the higher elevation the higher the mean streamwise velocity then the higher generated rotor torque and power. From the theory the trend should follow the magnitude of the mean streamwise velocity but this is not always the case and thus other factors should be considered.

In analyzing turbulence the standard deviation values are more important in quantifying the levels of turbulence. The higher the standard deviation of the instantaneous velocities, the higher the variance from which normal stresses are defined and hence the higher the turbulent kinetic energy. The results are presented in the form of the histogram plots.

Wind turbine 8 is expected to have the highest mean streamwise velocity at the hub height given that it has the highest elevation. Wind turbine 1 is expected to have the second highest streamwise mean velocity. However, wind turbine 7 which has a very low elevation is the second in line. This maybe explained due to the effect of the complex topography . Except for wind turbine 3 the mean values of streamwise velocity at the hub height in the heterogeneous forest are higher than those in the homogeneous forest. (See Fig. 4.12)

The standard deviation of the streamwise velocity vary inversely proportional to the mean values. It is observed that the standard deviation values of the streamwise velocity in the homogeneous forest are higher than the standard deviation values in the heterogeneous forest.

The mean values of the vertical wind velocity are seen to be in the downward direction in Fig. 4.13 of all the wind turbines and this maybe explained as a result of the complex terrain and forest canopies on the flow field.

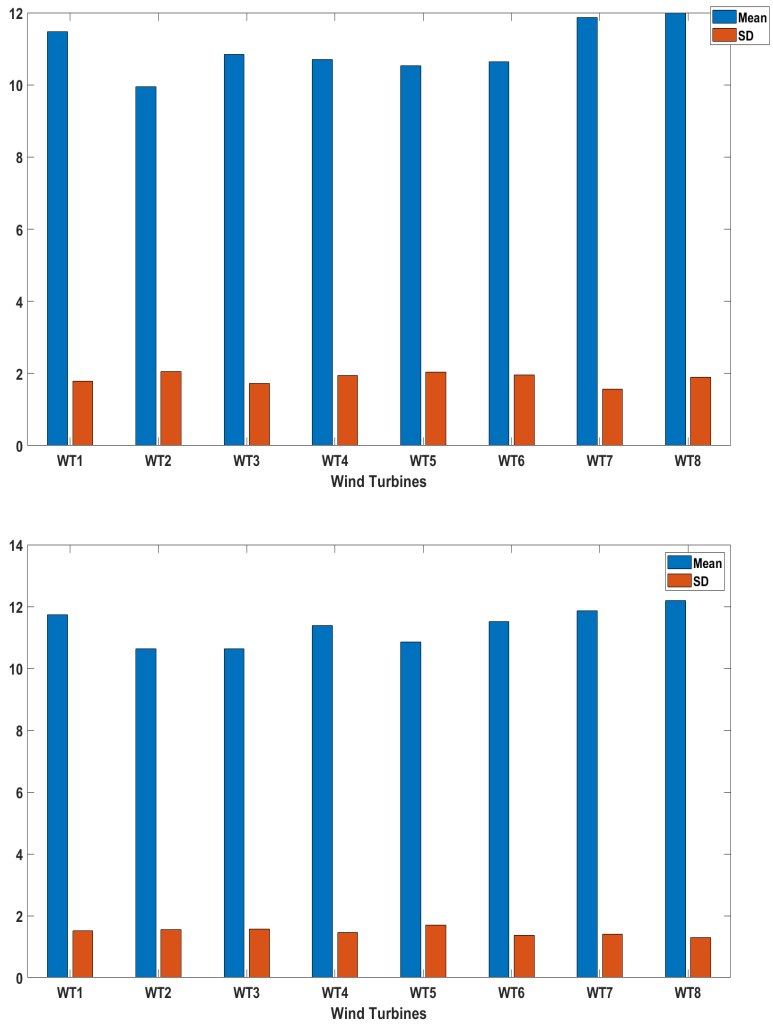

Figure 4.12: Mean and Standard deviation of streamwise velocity $\overline{u}$ at the hub height of Homogeneous (top) and Heterogeneous (bottom) forest.

The blade pitch angle vary proportionally with the streamwise mean velocity as seen in Fig. 4.15. It is observed in both forest cases. In addition the mean values of blade pitch angle in the heterogeneous forest are higher than mean values of the homogeneous forest. Wind turbine 8 in both cases has the highest mean and standard deviation. A higher standard deviation value has a destructive impact on the wind turbine as higher standard deviation tend induce higher fatigue loading.

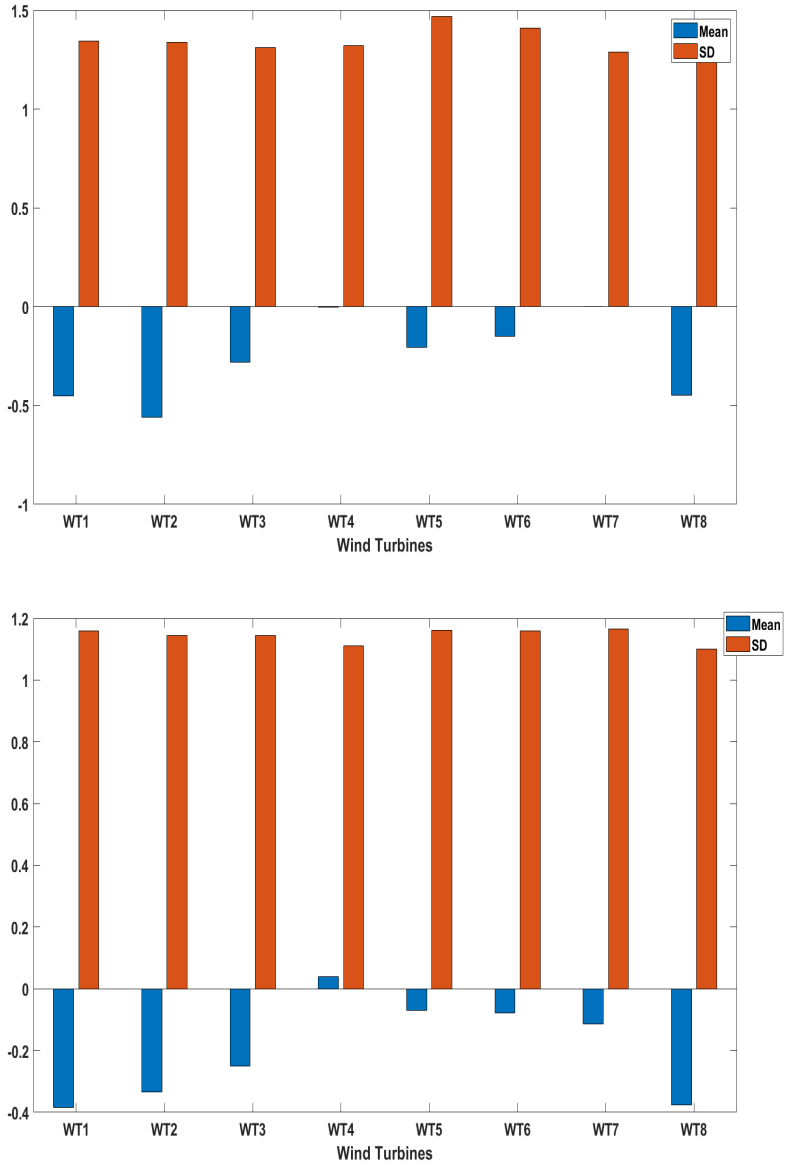

Figure 4.13: Mean and Standard deviation of vertical velocity $\overline{v}$ at the hub height of Homogeneous (top) and Heterogeneous (bottom) forest.

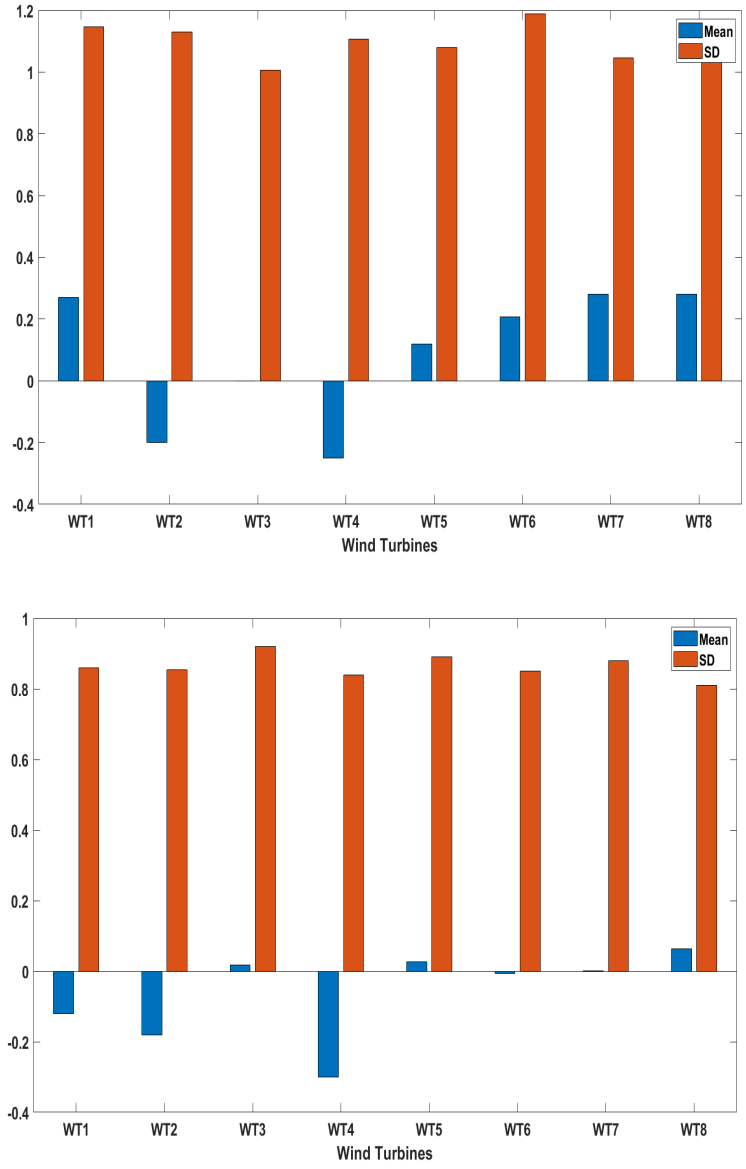

Figure 4.14: Mean and Standard deviation of spanwise velocity $\overline{w}$ at the hub height of Homogeneous (top) and Heterogeneous (bottom) forest.

Except for wind turbine 3 and 8 it is observed that the standard deviation values in the heterogeneous forest are higher than those in the homogeneous forest.

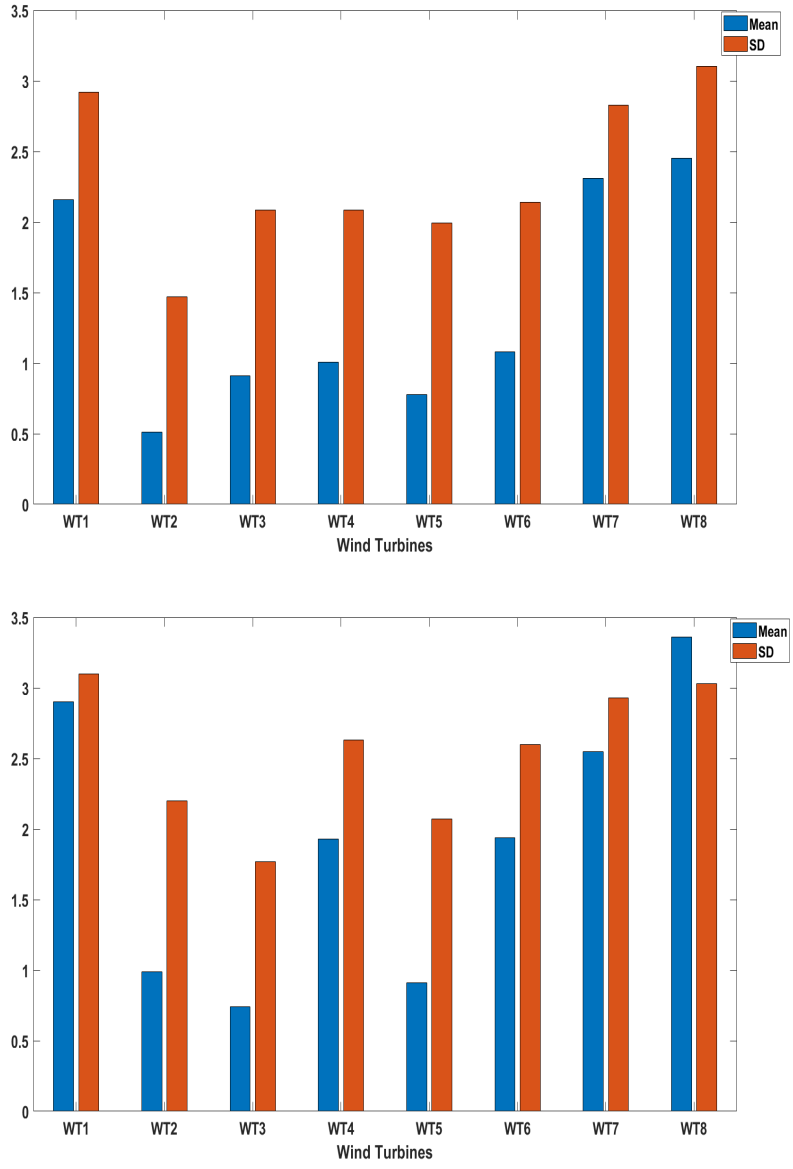

Figure 4.15: Mean and Standard deviation of blade pitch angles of Homogeneous (top) and Heterogeneous (bottom) forest.

Figure 4.16 shows that the generated torque vary linearly with the streamwise mean velocity. It is also observed that the mean values of the heterogeneous forest are higher than the mean values of the homogeneous forest except for wind turbine 3. The standard deviation values vary inversely with the mean values. The standard deviation values of the homogeneous forest are seen to be higher than for the heterogeneous forest except for wind turbine 3 and 7.

The rolling moment (Mx) mean and standard deviation values are presented in Fig.

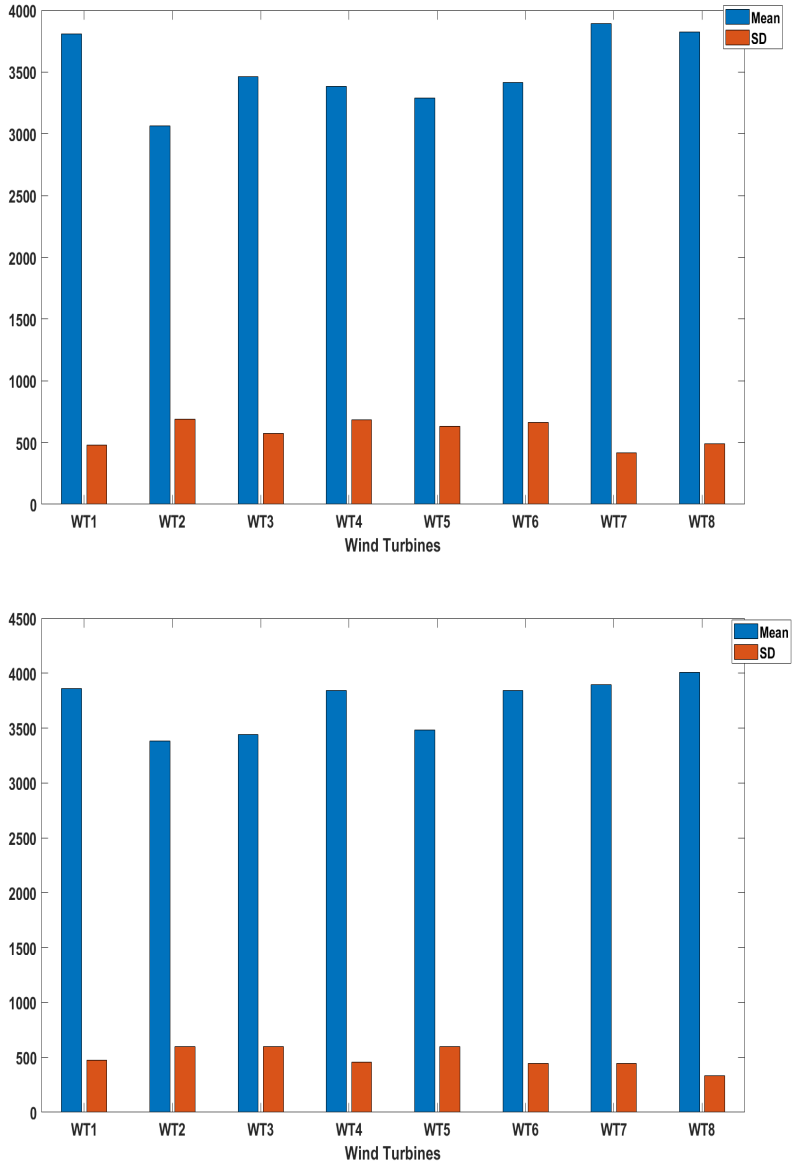

Figure 4.16: Mean and Standard deviation of generated rotor torque of Homogeneous (top) and Heterogeneous (bottom) forest.

4.17. It is seen that the mean values in the heterogeneous forest are higher than the mean values in the homogeneous forest except for wind turbine 3 and 7. The standard deviation values vary inversely proportional to the mean values. The standard deviation values in the homogeneous forest are higher than in the heterogeneous forest except for wind turbine 7.

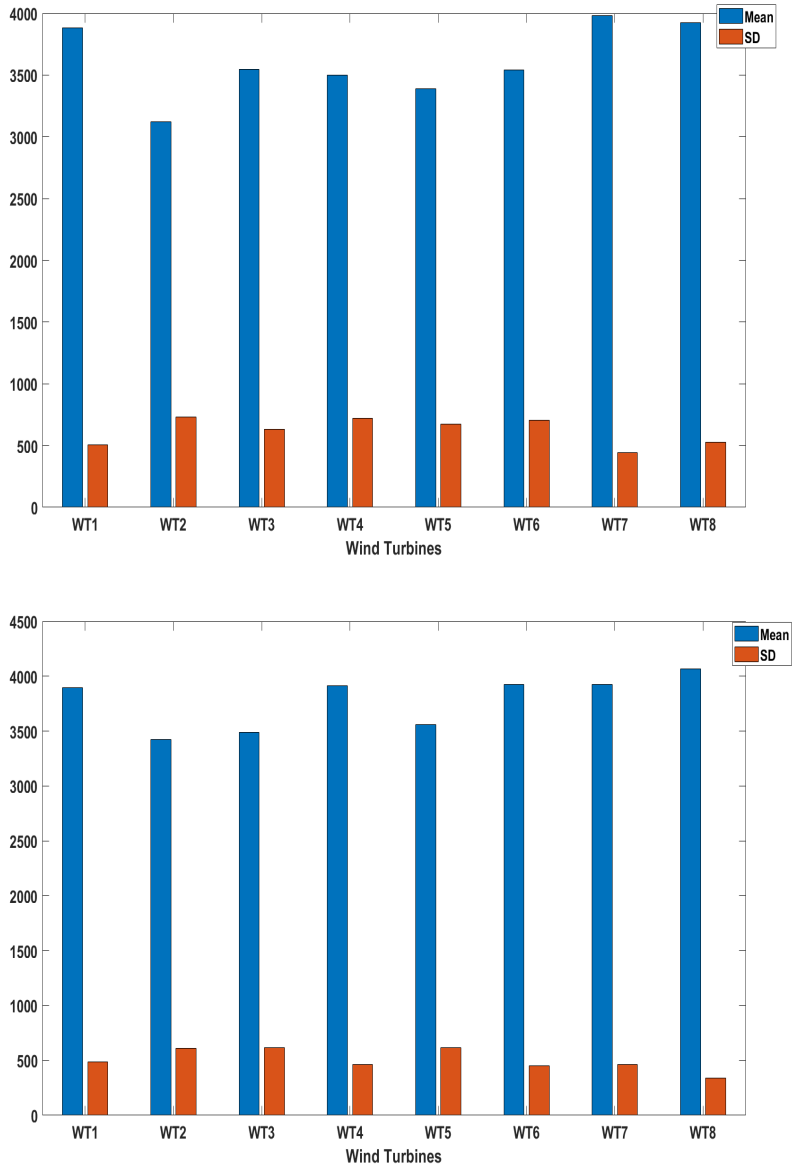

Figure 4.17: Mean and Standard deviation of rolling moment (Mx) for Homogeneous (top) and Heterogeneous (bottom) forest.

For the pitching moment (My) it is seen in Fig. 4.18 that the mean values of the homogeneous forest are higher than the mean values in the heterogeneous forest. For the heterogeneous forest it is observed that the mean values are in the reverse order with the mean values of streamwise velocity at hub height. The standard deviation values of the homogeneous forest are also higher than those in the heterogeneous

forest.

For the yawing moments (Mz) in Fig. 4.19 it is observed that the mean values of the homogeneous forest are greater than the mean values in the heterogeneous forest. It is also observed that the standard deviation values in the homogeneous forest are higher than the standard deviation values in the heterogeneous forest.

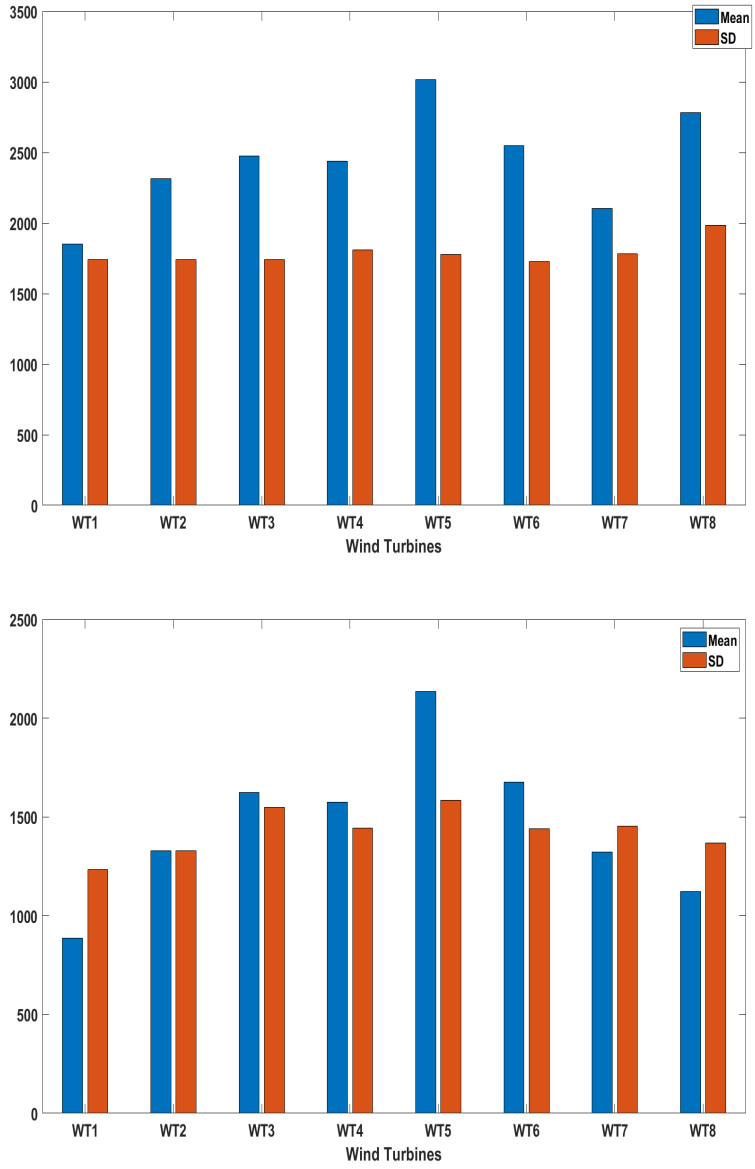

Figure 4.18: Mean and Standard deviation of pitching moment (My) for Homogeneous (top) and Heterogeneous (bottom) forest.

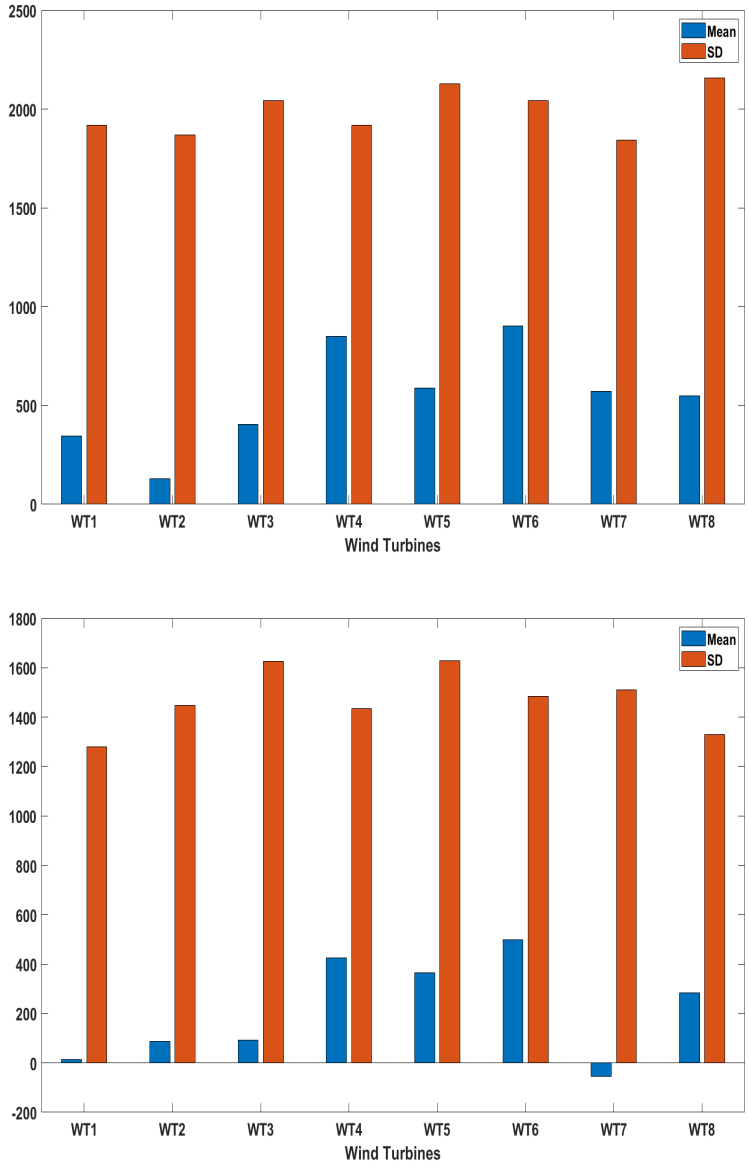

Figure 4.19: Mean and Standard deviation of yawing moment (Mz) for Homogeneous (top) and Heterogeneous (bottom) forest.

5
Conclusion

In this study, using LES the neutral ABL is modeled over a heterogeneous forest wind farm. For comparison reasons the wind farm in a homogeneous forest is modeled as well. After importing the instantaneous velocity field data to the wind turbine simulator *FAST* the dynamic response of the wind turbines are analyzed.

Results from the LES simulations show that both simulation cases (heterogeneous and homogeneous forest modeling) reach the fully developed condition so LES did a good job in flow modeling. Figure 4.1 stresses the influence of the forest canopy distribution between the two forests that depending on the location of the wind turbine in the heterogeneous forest, the streamwise velocity will vary close to the ground as opposed to that in the homogeneous forest. From Fig. 4.5 it is observed that the homogeneous forest assumption over-predicts turbulent kinetic energy levels the wind turbines are subjected to compared to the turbulent kinetic energy levels in the heterogeneous forest.

Furthermore from the aero-elastic solver, results show that the elevations of the wind turbines don't primarily dictate the magnitude of the streamwise mean wind speed (that is the higher the elevation the higher the streamwise mean wind speed). This is due to the effect of the complex terrain topography of the Röbergskullen wind farm. The mean of the streamwise velocity at hub height are seen to be higher for the heterogeneous forest compared to the homogeneous forest (Fig. 4.12). This is due to the acceleration of the flow in the heterogeneous forest (Fig. 4.1) compared to that of homogeneous forest. As a consequence of this the mean of the streamwise velocity, blade pitch angles, rolling moment (Mx) and the generated rotor torque in the heterogeneous forest are higher than the mean of the same signals in the homogeneous forest.

Except for the blade pitch angle signal the standard deviation of streamwise velocity, rolling moment (Mx), pitching moment (My), yawing moment (Mz) and generated rotor torque are seen to be higher in the homogeneous forest compared to the heterogeneous forest. Thus except for blade pitch angle the standard deviation values of the mentioned signals show a correlation with turbulent kinetic energy that is the higher the standard deviation the higher the turbulent kinetic energy

The homogeneous forest modeling assumption is thus seen to predict higher turbulence a wind turbine is subjected to when placed in such a forest model compared to the realistic heterogeneous forest modeling approach.

Bibliography

[1] (2017). *STAR-CCM+* Documentation. Siemens PLM Software.

[2] Buresti G., (2012). *Elements of Fluid Dynamics*. Imperial College Press.

[3] Bechmann, A., (2006). *Large-eddy Simulation over Complex Terrain*. RisøNational Laboratory. Risø-PhD-28(EN).

[4] Brekason, K. (2018). *CFD Modeling of a Neutral Atmospheric Boundary Layer over Complex Terrain*. Chalmers University of Technology, Goteborg, Sweden.

[5] Davidson, L. (2020). Fluid mechanics, turbulent flow and turbulence modeling. http://www.tfd.chalmers.se/ lada/ Accessed: 2019-11-05.

[6] Ferziger, J.H., Peric, M. (2002). *Computational Methods for Fluid Dynamics*. Springer ISBN 978-3-540-42074-3.

[7] Gerasimov, A. (2016). Quick Guide to Setting Up LES-type Simulations, version 1.4. European Technology Group, Ansys, Sweden.

[8] Hau, E. (2012). *Wind Turbines*. Springer e-ISBN 978-3-642-27151-9.

[9] Hosoi, F. Omasa K. (2009). Estimating vertical plant area density profile and growth parameters of a wheat canopy at different growth stages using three-dimensional portable lidar imaging. *ISPRS Journal of Photogrammetry and Remote Sensing*, 64 (2009) 151–158

[10] Ingram, G. (2018). *Wind Turbine Blade Analysis using the Blade Element Momentum Method*. Durham University, Durham, England

[11] Jonkman, J., Butterfield, S., Musial, W., Scott, G. (2009). Definition of a 5MW reference wind turbine for offshore system development. Technical report, National Renewable Energy Lab.(NREL), Golden, CO (United States).

[12] Jonkman, J. M., Buhl Jr, M. L., et al. (2005). Fast user's guide. National Renewable Energy Laboratory, Golden, CO, Technical Report No. NREL/EL-

500-38230.

[13] Kaimal,J.C., Finnigan J.J (1994). *Atmospheric Boundary Layer Flows*. Oxford University Press, 1994. ISBN 0-19-506239-6

[14] Kandt, J. (2019). Current Limitations of Integrating CFD and Structural Analyses for the Design of Offshore Wind Turbines. Chalmers University of Technology, Goteborg, Sweden.

[15] Kaveh, A. Sabeti, Sepehr. (2019). Optimal Design of Jacket supporting structures for offshore wind turbines using enhanced colliding bodies optimization algorithm.

[16] Manwell J.F., Mcgowan J.G., Rogers A.L. (2009). *Wind Energy Explained*. Wiley ISBN 978-0-470-01500-1.

[17] NWTC Information Portal (FAST). https://nwtc.nrel.gov/FAST. Last modified 04-January-2018 ; Accessed 14-April-2020

[18] Nebenführ, B., Davidson, L.(2017). Prediction of wind-turbine fatigue loads in forest regions based on turbulent LES inflow field. DOI: 10.1002/we. Wind Energy (20:1003–1015).

[19] Rathinasamy, S (2018). *Comparison between wind turbines in forestall and flat areas of Sweden*. Halmstad University, Halmstad, Sweden.

[20] Taylor, P.A., Teunissen, H.W. (1983) Askervein '82: Report on the September/October 1982 Experiment to Study Boundary Layer Flow Over Askerveint, South Uist. Atmospheric Environment Service, Downsview, Ontario (Report MSRB-83-8).

[21] Taylor, P.A., Teunissen, H.W. (1985) The Askervein Hill Project: Report on the September/October 1983 Main Field Experiment. Atmospheric Environment Service, Downsview, Ontario (Report MSRB-84-86).

A

Appendix 1

A.1 Wind Measurements over Rödbergskullen Wind Farm

Measurements of wind data were taken over the meteorological mast located at the Rödbergskullen Wind Farm. The measurements were taken at hourly rate for the year 2016 at a height of 60m a.g.l include the average and standard deviation of wind speed and direction. Dominating wind speed, turbulent intensity and wind direction data were also taken. The dominating wind speeds were in the range 6-8m/s in the direction of 225° with respect to the North with a turbulent intensity of 13% [4].

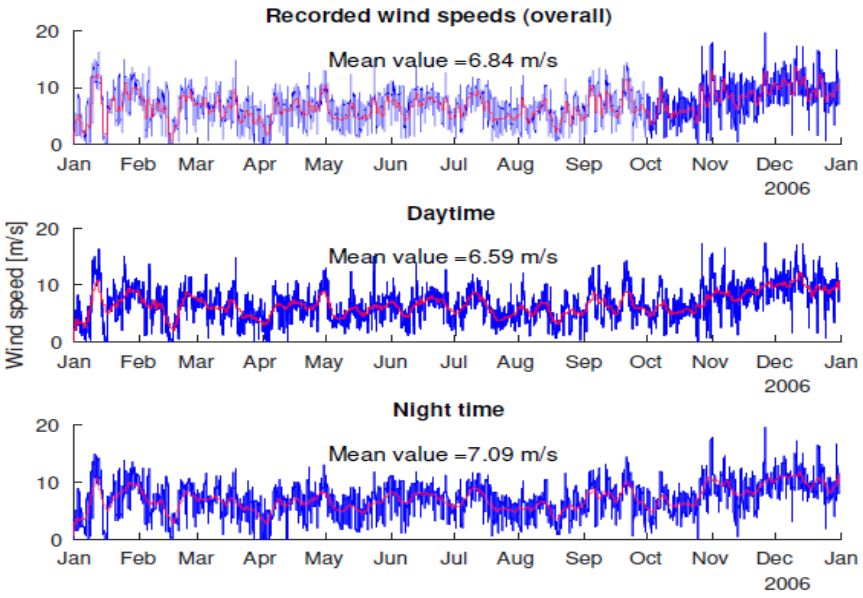

Figure A.1: Wind speed average measurements over Rödbergskullen. The figure shows overall recorded values and compares them to the values recorded only during the day and during the night. The blue lines indicate measured values while the red lines indicate 72 hour average [4].

Figure A.1 shows the average wind speed of the Rödbergskullen Wind Farm. The topmost are the overall measurements recorded and the bottom are the same results filtered to show the daytime and night time speed. Both indicate speeds close to 7m/s indicating that there isn't much difference in wind speed between daytime and

nighttime. A histogram plot is shown in Fig.A.2 which further indicates that the most dominating wind speeds lie in the range between 6-8m/s. 40% of the time the wind speeds are in the range of 5-8m/s [4].

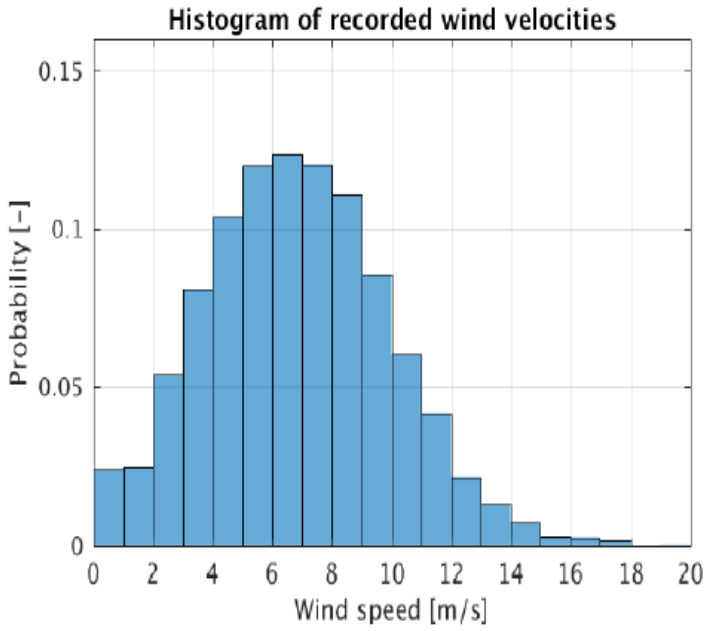

Figure A.2: Histogram of recorded wind speed averages [4].

The measured wind direction suggests that dominating winds are heading in a south-westerly direction of roughly 225°. Figure A.3 shows the distribution of wind direction too.

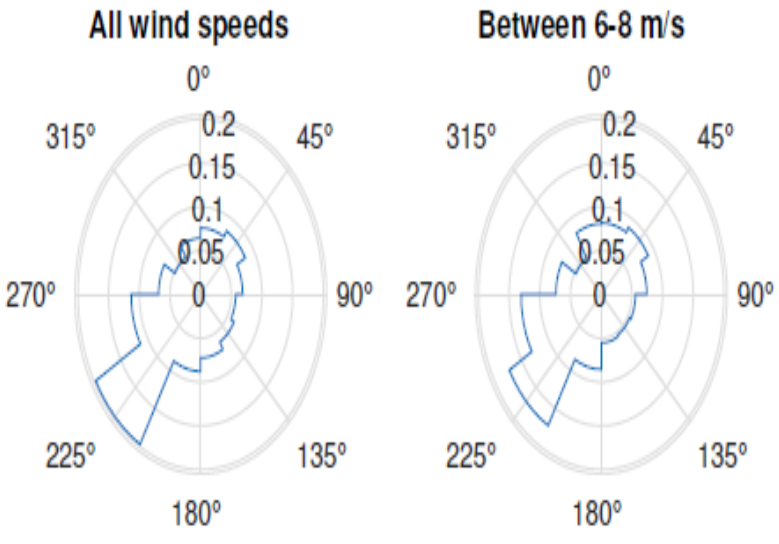

Figure A.3: Wind Direction [4].

Figure A.4 displays the turbulent intensity as a function of wind speeds. The turbulent intensity decreases as velocity increases and with higher speeds there is a lower variance. Above speeds of 6m/s the turbulent intensity becomes almost constant with a value of 13% [4].

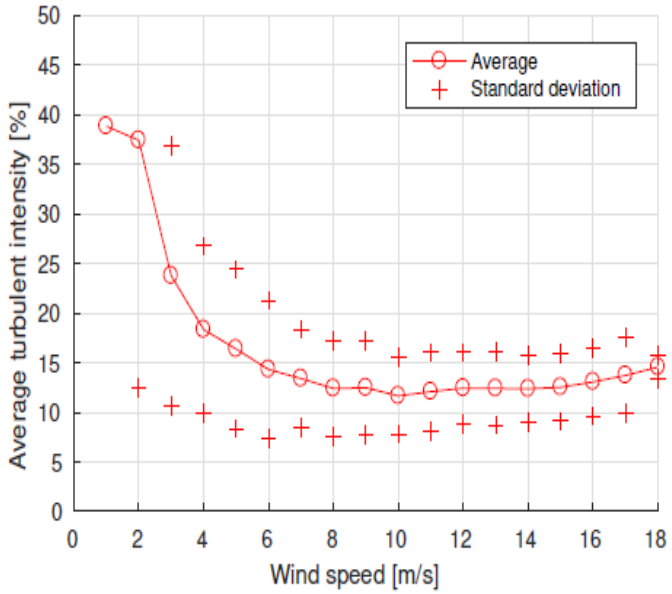

Figure A.4: Turbulent Intensity [4].

The topography of the wind farm and the area around it is presented in Fig. A.5 where the lowest to the highest elevation varies from 334m to 542m.

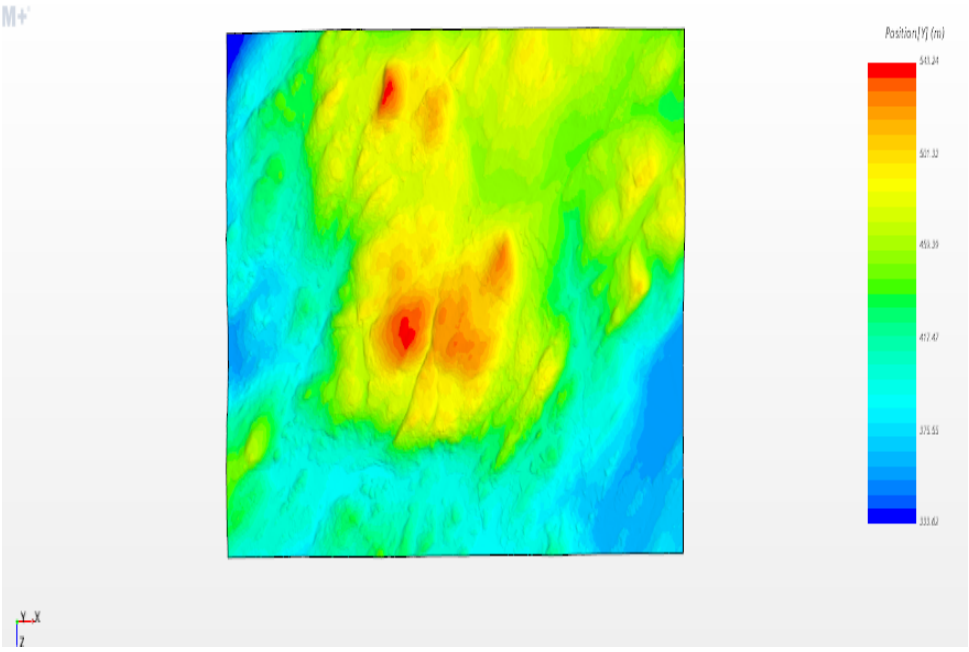

Figure A.5: Topography of the area.